eNeuro

Research Article: Confirmation | Development

Grp94 regulates the recruitment of aneural AChR clusters for the assembly of postsynaptic specializations by modulating ADF/cofilin activity and turnover

https://doi.org/10.1523/ENEURO.0025-20.2020

Cite as: eNeuro 2020; 10.1523/ENEURO.0025-20.2020

Received: 26 January 2020
Revised: 27 July 2020
Accepted: 27 July 2020

1. Manuscript Title (50 word maximum)
Grp94 regulates the recruitment of aneural AChR clusters for the assembly of postsynaptic specializations by modulating ADF/cofilin activity and turnover

2. Abbreviated Title (50 character maximum)
Grp94 regulates postsynaptic development at NMJs

3. List all Author Names and Affiliations in order as they would appear in the published article
Zora Chui-Kuen Chan*, Linyan Deng*, Chi Wai Lee
School of Biomedical Sciences, Li Ka Shing Faculty of Medicine, The University of Hong Kong, Hong Kong
* Equal contribution

4. Author Contributions: ZCC, LD, and CWL performed experiments and analyzed data. CWL wrote the manuscript and supervised the study.

5. Correspondence should be addressed to (include email address)
Chi Wai Lee, School of Biomedical Sciences, The University of Hong Kong
L4-63, Lab Block, 21 Sassoon Road, Pokfulam, Hong Kong. Email: chiwai.lee@hku.hk

6. Number of Figures: 6 (Main Figures) + 7 (Extended Data)

7. Number of Tables: 1

8. Number of Multimedia: 0

9. Number of words for Abstract: 241

10. Number of words for Significance Statement: 119

11. Number of words for Introduction: 708

12. Number of words for Results: 3446

13. Number of words for Discussion: 1853

14. Acknowledgements: The authors acknowledge the assistance of Proteomics and Metabolomics Core and Imaging Core, Centre for PanorOmic Sciences at HKU Medicine.

15. Conflict of Interest: Authors report no conflict of interest

16. Funding sources: This project was partly supported by the Early Career Grant (27102316) and General Research Fund (17100718 and 17100219) from Research Grants Council of Hong Kong, the Health and Medical Research Fund (04151086) from Food and Health Bureau of Hong Kong, and the Seed Fund Programme for Basic Research from The University of Hong Kong (201601159003, 201711159098, and 201811159078) to CWL.

ABSTRACT

Temperature is a physiological factor that affects neuronal growth and synaptic homeostasis at the invertebrate neuromuscular junctions (NMJs); however, whether temperature stress could also regulate the structure and function of the vertebrate NMJs remains unclear. In this study, we use *Xenopus laevis* primary cultures as a vertebrate model system for investigating the involvement of heat shock protein 90 (HSP90) family of stress proteins in NMJ development. Firstly, cold temperature treatment or HSP90 inhibition attenuates the formation of aneural acetylcholine receptor (AChR) clusters, but increases their stability after they are formed, in cultured muscles. HSP90 inhibition specifically affects the stability of aneural AChR clusters and their associated intracellular scaffolding protein rapsyn, instead of causing a global change in cell metabolism and protein expression in *Xenopus* muscle cultures. Upon synaptogenic stimulation, a specific HSP90 family member, glucose-regulated protein 94 (Grp94), modulates the phosphorylation and dynamic turnover of actin depolymerizing factor (ADF)/cofilin at aneural AChR clusters, leading to the recruitment of AChR molecules from aneural clusters to the assembly of agrin-induced postsynaptic specializations. Finally, postsynaptic Grp94 knockdown significantly inhibits nerve-induced AChR clustering and postsynaptic activity in nerve-muscle co-cultures as demonstrated by live-cell imaging and electrophysiological recording, respectively. Collectively, this study suggests that temperature-dependent alteration in Grp94 expression and activity inhibits the assembly of postsynaptic specializations through modulating ADF/cofilin phosphorylation and activity at aneural AChR clusters, which prevents AChR molecules from being recruited to the postsynaptic sites via actin-dependent vesicular trafficking, at developing vertebrate NMJs.

SIGNIFICANCE STATEMENT

HSP90 is one of the most studied and abundant molecular chaperones of eukaryotic cells that protect proteins from cellular stress. Our study provides the first evidence showing that temperature-dependent alteration in the expression and activity of a specific HSP90 family member Grp94 regulates the recruitment of aneural AChR clusters for the assembly of postsynaptic specializations through ADF/cofilin-mediated vesicular trafficking at developing vertebrate NMJs. Given the recent identification of Grp94 and other ER chaperones as potential biomarkers for diagnosis of myasthenia gravis, an autoimmune NMJ disease, results of this study not only enhance our understanding on the fundamental mechanisms underlying NMJ development, but also provide insights into the pathogenic mechanisms underlying ER stress response and NMJ disruption in neuromuscular diseases.

INTRODUCTION

Synapses are the fundamental structures in the nervous system that enable efficient communication between neurons and their target cells. Neuromuscular junction (NMJ), a peripheral synapse, is formed between a motor neuron and a skeletal muscle fiber. Due to its accessibility and simplicity in structure, NMJ has served as a model synapse for elucidating the molecular mechanisms underlying synapse formation and maintenance in health, disease, and aging (Sanes and Lichtman, 2001; Li et al., 2018; Chan et al., 2020a). At developing NMJs, aggregation of acetylcholine receptors (AChRs) at the postsynaptic membranes represents an important step in neuromuscular synaptogenesis. Before nerve innervation, AChR molecules are both diffusely distributed throughout the muscle surface and spontaneously clustered in the form of AChR pre-patterns (Yang et al., 2000; Lin et al., 2001; Yang et al., 2001). Upon synaptogenic induction, nerve-induced AChR clustering at the postsynaptic sites is believed to be contributed by the recruitment of both diffuse and pre-patterned AChRs, as well as the local synthesis of AChR proteins at the sub-synaptic nuclei (Sanes and Lichtman, 2001). The postsynaptic specializations at NMJs are associated with dense networks of stable filamentous actin (F-actin) structures at the cell cortex, which mediate AChR cluster formation and redistribution through rapsyn (Dai et al., 2000; Borges and Ferns, 2001; Dobbins et al., 2008). A previous study has demonstrated that actin depolymerizing factor (ADF)/cofilin-mediated actin dynamics regulate the vesicular trafficking of AChRs at developing NMJs (Lee et al., 2009). These findings suggest a novel ADF/cofilin-dependent transcytosis mechanism underlying the redistribution of aneural AChR clusters for the assembly of synaptic AChR clusters at NMJs. However, the mechanistic regulation of AChR redistribution from aneural to synaptic clusters at developing NMJs remains unclear.

Heat shock proteins (HSPs) are molecular chaperones that show remarkable sequence homology across the phylogenetic spectrum from a unicellular organism, *S. cerevisiae*, to a multicellular organism, mammal. These stress proteins are grouped into major families according to their approximate molecular weight in kDa. Among them, HSP90 is a highly abundant and ubiquitous molecular chaperone, which plays an essential role in many different processes to maintain cellular homeostasis under stressful conditions (Schopf et al., 2017). The HSP90 family includes cytosolic HSPs (HSP90α and HSP90β), endoplasmic reticulum (ER)-resident glucose-regulated protein 94 (Grp94), and mitochondrial-specific tumor necrosis factor

receptor-associated protein-1 (TRAP-1). Grp94, encoded by the HSP90B1 gene, shares many biochemical features with other HSP90 proteins (Csermely et al., 1998; Marzec et al., 2012). It is believed that Grp94 can escape ER retention and retrieval in cells under ER stress (Gutierrez and Simmen, 2014). Intriguingly, a previous study suggested that Grp94 can also be found in the cell surface of C2C12 myotubes, in which Grp94 phosphorylation mediated by the Src kinase Fyn promotes the chaperone export from the ER during the early phase of myoblast differentiation (Frasson et al., 2009). Given that the cytosolic HSP90β is known to regulate AChR cluster formation and maintenance through modulating rapsyn turnover (Luo et al., 2008), whether the ER-resident HSP90 family member, Grp94, is involved in NMJ development remains unknown.

In this study, we first show that temperature stress up-regulates the mRNA transcript levels of both HSP90β and Grp94, but down-regulates the protein level of only Grp94, in cultured *Xenopus* muscle cells. Interestingly, pharmacological inhibition of HSP90 activity by 17-(allylamino)-17-demethoxygeldanamycin (17-AAG) or molecular manipulation of endogenous Grp94 expression suppresses the formation of aneural AChR clusters and increases the stability of aneural AChR clusters after they are formed. Upon synaptogenic stimulation, the recruitment of pre-existing AChRs to agrin-induced AChR clusters is significantly reduced in wild-type muscle cells treated with 17-AAG and in Grp94 knockdown muscle cells. Interestingly, 17-AAG treatment accelerates the turnover of green fluorescent protein-tagged *Xenopus* ADF/cofilin (GFP-XAC) at both perforated and AChR-rich regions of aneural clusters resembling the dynamic turnover of GFP-XAC inactive (S3E) mutant, suggesting that HSP90 regulates dephosphorylation and activation of ADF/cofilin. Finally, nerve-induced AChR clustering and synaptic functions are impaired in chimeric nerve-muscle co-cultures containing Grp94 knockdown muscles and wild-type neurons, indicating the essential roles of postsynaptic Grp94 in regulating synaptic structure and function of developing NMJs. Together, our study suggests that temperature-dependent alteration in Grp94 expression and activity regulates the recruitment of AChR molecules from aneural to agrin-induced synaptic clusters through modulating ADF/cofilin phosphoregulation to mediate actin-dependent vesicular trafficking at developing NMJs.

MATERIALS AND METHODS

Embryo Microinjection and Primary Culture from *Xenopus* Embryos

Adult female frogs (Xenopus 1, RRID: XEP_Xla100) were injected with 1000 I.U. human chorionic gonadotropin (hCG, Sigma, Cat# CG10) with 0.1% BSA to induce ovulation. After fertilization *in vitro*, embryos were maintained in Holtfreter's solution (vol/vol; 60 mM NaCl, 0.6 mM KCl, 0.9 mM $CaCl_2$, 0.2 mM $NaHCO_3$, pH 7.4). 20-100 pg of DNA constructs encoding either wild-type or phosphorylation mutant forms (S3A and S3E) of GFP-XAC (gifts from Dr James Bamburg, Colorado State University) were microinjected into one blastomere of 1- or 2-cell stage *Xenopus* embryos with an oocyte injector. GFP-expressing embryos were screened for primary culture preparation. Myotomal muscle tissues and neural tubes were isolated from stage 19-22 *Xenopus* embryos after enzymatic digestion with 1 mg/ml collagenase (Sigma-Aldrich, Cat# C98191G), followed by dissociation with calcium-magnesium-free solution. Dissociated muscle cells were then plated on glass bottom dishes or glass coverslips coated with entactin-collagen IV-laminin (ECL) cell attachment matrix (Merck Millipore, Cat# 08-100). The ECL coating was performed by incubating the coverslips or dishes with 10 µg/ml ECL in 10% Leibovitz's L-15 medium (Sigma-Aldrich, Cat# L4386) at 37°C for 3 hours. The coating was later washed with phosphate-buffered saline (PBS) solution (137 mM NaCl, 2.7 mM KCl, 10 mM Na_2HPO_4, 1.8 mM KH_2PO_4), followed by Steinberg's solution (60 mM NaCl, 0.67 mM KCl, 0.35 mM $Ca(NO_3)_2$, 0.83 mM $MgSO_4$, 10 mM HEPES, pH 7.4). Cells were cultured in medium containing 87% (vol/vol) Steinberg's solution, 10% (vol/vol) Leibovitz's L-15 Medium, 1% fetal bovine serum (Gibco, Cat# 10270), 1% penicillin/streptomycin (Thermo Fisher Scientific, Cat# 15140122) and 1% gentamicin sulfate (Thermo Fisher Scientific, Cat# 15750060). Muscle cells were kept at 22°C for at least 24 hours to allow cell attachment and aneural AChR cluster formation before treatments, if any. To make nerve-muscle or bead-muscle co-culture, dissociated spinal neurons or polystyrene latex beads coated with agrin (R&D Systems, Cat# 550-AG-100/CF) were added in 2-d old muscle cultures and maintained for 1 d before imaging. All the experiments involving *Xenopus* frogs and embryos were performed in accordance with the [Author University] animal care committee's regulations.

Morpholino-Mediated Knockdown of Endogenous Proteins

Knockdown of endogenous proteins in *Xenopus* was achieved by embryonic injection of antisense morpholino oligonucleotides (MO, Gene Tools), which bind to the target mRNA sequence that block its protein translation. The following MO sequences were used in this study: *Xenopus* Grp94 MO: 5'-GACCGATTGCCCAAAACTTCCTCAT-3', *Xenopus* HSP90β MO: 5'-CATTGTGGGCAACTTCTGGCATC-3', and control MO: 5'-CCTCT TACCT CAGTT ACAAT TTATA-3'. To visualize the presence of MO in the microinjected embryos, MOs were co-injected with Alexa Fluor 488-conjugated dextran (Thermo Fisher Scientific, Cat# D22910) as a cell lineage tracer. The effectiveness of MO-mediated knockdown of endogenous proteins was validated by Western blot analyses.

Quantitative Real-Time RT-PCR Analysis of HSP90 Expression

Total RNA was extracted using the TRIzol reagent from 2-d old *Xenopus* muscle cultures incubated at 22°C, 15°C, or 10°C, respectively. Isolated RNA samples were treated with DNase (Thermo Fisher Scientific, Cat# EN0521) to remove genomic DNA. An equal amount of RNA from samples was reverse transcribed into cDNA with High-Capacity cDNA Reverse Transcription Kit (Thermo Fisher Scientific, Cat# 4368814) and qPCR was performed using CXF96 Touch together with SYBR Premix Ex Taq (Takara Bio, Cat# RR420A). Data were acquired and analysed with CFX Manager (Bio-Rad, RRID: SCR_017251). Primers are listed below:

HSP90α - Forward: 5'-TCTGACTGACCCAAGCAAAC-3'
HSP90α - Reverse: 5'-GCCTGCAAAGCCTCCATAAA-3'
HSP90β - Forward: 5'-CTATGATTGATACCGGAATT-3'
HSP90β - Reverse: 5'-CATATTGCTCATCATCATTG-3'
Grp94 - Forward: 5'-CACTGATGACCCTCGTGGTG-3'
Grp94 - Reverse: 5'-AGGGGCTCCTCTACTGTCTC-3'
TRAP-1 - Forward: 5'-CCCAGGGACAAAGGTTGTGA-3'
TRAP-1 - Reverse: 5'-TCATGCTGCCATTCCCCAAT-3'
GAPDH - Forward: 5'-GTGTATGTGGTGGAATCT-3'
GAPDH - Reverse: 5'-AAGTTGTCGTTGATGACCTTTGC-3'

Pharmacological Treatment

For experiments studying the effect of HSP90 on aneural AChR cluster formation, muscle cultures were pre-treated with different concentrations (0.1 nM, 0.25 nM, or 1 nM) of 17-AAG (ApexBio, Cat# A4054-10). To investigate the effect of HSP90 in the remodeling of AChR clusters, 2-d old muscle cultures were treated with 17-AAG (1 nM) or PU-WS13 (15 μM) (ApexBio, Cat# B5885). For experiments investigating the contribution of aneural AChR clusters to agrin-induced synaptic AChR clusters, 2-d old muscle cells were treated with 17-AAG (1 nM) from 1 h prior to photobleaching experiments. For the experiments investigating the nerve-induced AChR clusters, PU-WS13 (15 μM) was applied to 2-d old muscle cultures from 1 h prior to spinal neurons plating. For experiment investigating inhibition of HSP90 activity on rapsyn localization in aneural AChR clusters, 2-d old muscle cultures were treated with 1 nM 17-AAG from 1 h prior to agrin bead addition. For experiments investigating the HSP90 and Grp94 activity in rapsyn localization and AChR internalization, 2-d old muscle cultures were treated with 1 nM 17-AAG or 15 μM PU-WS13 from 1 h before plating spinal neurons or adding agrin beads.

Labeling of Different AChR Pools in Cultured Muscle Cells

To differentially identify the pre-existing and newly synthesized AChRs, surface AChRs in 2-d old muscle cultures were first labeled with 0.1 μM tetramethylrhodamine- (Rh-, Thermo Fisher Scientific, Cat# T1175), Alexa Fluor 488- (488-, Thermo Fisher Scientific, Cat# B13422), or Alexa Fluor 647- (647-, Thermo Fisher Scientific, Cat# B35450) conjugated α-bungarotoxin (BTX) for 45 min, followed by extensive washing with culture medium. Cells were then saturated with a high dose of unconjugated α-bungarotoxin (6 μM, Thermo Fisher Scientific, Cat# B1601) for 30 mins, followed by extensive washing with culture medium. Newly synthesized and inserted AChRs were then labeled with 1 μM Alexa Fluor 488- or 647-conjugated α-bungarotoxin at different timepoints, as specified. For live imaging, glass coverslips with culture cells were mounted on sealed live chamber containing culture medium. To determine the density of surface AChRs, cultured muscle cells were first labeled with 0.2 μM biotin-XX-conjugated α-bungarotoxin (biotin-BTX, Thermo Fisher Scientific, Cat# B1196) for 45 min, then fixed with 4% paraformaldehyde in PBS for 15 min and permeabilized with 0.5% Triton X-100 in PBS for 10 min. The samples were then incubated with 0.16 μM Qdot 655 (QD)-conjugated streptavidin (Thermo Fisher Scientific, Cat# Q10143MP) for 10 min. For

experiments testing the possibility of AChR photo-dissipation, surface AChRs were labeled with 1 μM Alexa Fluor 594-BTX (594-BTX, Thermo Fisher Scientific, Cat# B13423) or Rh-BTX for 45 min, followed by extensive washing with culture medium. After 6 or 24 h, newly inserted surface AChRs were labeled with 1 μM 488-BTX for 45 min. To differentially identify surface and internal AChRs, cells were first fixed with 4% paraformaldehyde in PBS for 15 min. Surface AChRs were labeled with 0.1 μM Rh-BTX for 45 min, followed by saturation with 6 μM unconjugated BTX for 30 mins. After cell permeabilization with 0.5% Triton X-100, internal AChRs were labeled with 0.1 μM 488-BTX for 45 min. Coverslips were then mounted on glass slides with the anti-bleaching reagent fluoromount-G (Thermo Fisher Scientific, Cat# 00-4958-02) for later observation.

Fixation and Immunostaining of Cells

Xenopus muscle cultures were fixed with 4% paraformaldehyde in PBS for 15 min. After extensive washing with PBS, fixed cells were permeabilized with 0.5% Triton X-100 in PBS, followed by blocking with 2% BSA at room temperature for 2 h or at 4°C overnight. Cells were incubated with primary antibodies, including *Xenopus* ADF/cofilin (1:500, a gift from Dr James Bamburg, Colorado State University), p34-Arc/ARPC2 (1:100; EMD Millipore, Cat# 07-227, RRID: AB_310447), rapsyn (1:100; Affinity Bioreagent, Cat# MA1-746, RRID: AB_2177611), or vinculin (1:250; Sigma-Aldrich, Cat# V4505, RRID: AB_477617) for 2 h, followed by fluorophore-conjugated secondary antibodies (Thermo Fisher Scientific, Cat# A-11029, RRID: AB_2534088; Cat# A-21206, RRID: AB_2535792) for 45 min. Coverslips were then mounted on glass slides with the anti-bleaching reagent fluoromount-G for later observation.

Quantitative Metabolomics

Extraction and Derivatization of Polar Metabolites

1000 μl methanol/water (80%, v/v) with 200 ng norvaline internal standard was added to the samples. The samples were homogenized after 2 cycles of sonication at 10 microns for 20 s on ice and 10 s pause time. The samples were centrifuged for 5 min at 16,000 g at 4°C. 500 μl supernatant was dried under a gentle stream of nitrogen at room temperature for derivatization. The dried residue was redissolved and derivatized for 2 h at 37°C in 40 μl methoxylamine

hydrochloride (30 mg/ml in pyridine), followed by trimethylsilylation for 1 h at 37°C in 70 µl MSTFA with 1% TMCS. Up to 1 µl sample was injected for GC-MS/MS analysis.

Extraction and Transesterification of Fatty Acid Metabolites

100 µl chloroform with 20 µg C19:0 fatty acid internal standard was spiked to the samples. The samples were homogenized after 2 cycles of sonication at 10 microns for 20 s on ice and 10 s pause time. The sample was centrifuged for 5 min at 16,000 g at 4°C. The pellet was separated and stored at -80°C. 1 ml methanol and 50 µl concentrated hydrochloric acid (35%, w/w) were added to the sample. The solution was overlaid with nitrogen and the tube was tightly closed. After vortexing, the tube was heated at 100°C for 1 h. Once cooled to room temperature, 1 ml hexane and 1 ml water were added for FAMEs extraction. The tube was vortexed and after phase separation, up to 1 µl the hexane phase was injected for GC-MS analysis.

Data acquisition

GC-MS chromatogram was acquired in SCAN and MRM mode in an Agilent 7890B GC-Agilent 7010 Triple Quadrapole Mass Spectrometer system (Santa Clara, CA, USA). For polar metabolites, the samples were separated through an Agilent (Santa Clara, CA, USA) DB-5MS capillary column (30 m x 0.25 mm ID, 0.25 µm film thickness) under constant flow at 1 ml min^{-1}. Characteristic quantifier and qualifier transitions were monitored in MRM mode during the run. For fatty acid metabolites, the samples were separated through an Aligent DB-23 capillary column (60 m x 0.25 mm ID, 0.15 µm film thickness) under constant pressure at 33.4 psi. Characteristic fragment ions (m/z 55, 67, 69, 74, 79, 81, 83, 87, 91, 93, 95, 96, 97, 115, 127, 143) were monitored in SIM mode throughout the run. Mass spectra from m/z 50-350 were acquired in SCAN mode. Principal component analyses (PCA) of polar metabolites and fatty acids was conducted with the determined data peaks using MetaboAnalyst 4.0 (Chong et al., 2019).

Protein Synthesis Assay

To determine the effects of HSP90 inhibition on protein synthesis in cultured *Xenopus* muscle cells, 1 nM 17-AAG was added to culture medium before cell plating. For the positive control, 4-d old muscle cells were treated with 25 µM cycloheximide (ApexBio, Cat# A8244-1000) for 2 h before adding O-propargyl-puromycin (OPP) reagent (Thermo Fisher Scientific, Cat# C10456). After 30 min, cells were fixed with 4% paraformaldehyde in PBS for 15 min and

permeabilized with 0.5% Triton X-100 in PBS, followed by OPP detection according to manufacturer's instructions.

Immunoblotting

To validate the effectiveness of MO-mediated knockdown of endogenous proteins, the dorsal parts from *Xenopus* embryos at Nieuwkoop and Faber stage 19 to 22 were homogenized in RIPA buffer (Thermo Fisher Scientific, Cat# 89900) containing 1% protease inhibitor cocktail and 1% EDTA. For experiments investigating the effects of temperature on HSP90β and Grp94 expression, 2-d old cultured muscle cells incubated at 22°C or 10°C were scraped and homogenized in RIPA buffer containing 1% protease inhibitor cocktail and 1% EDTA. Protein lysates were obtained from the supernatant after high-speed centrifugation (15,000x g). The concentration of protein lysates was determined by BCA protein assay kit (Thermo Fisher Scientific, Cat# 23227). 10-30 μg protein lysates, Pierce lane marker non-reducing sample buffer (25% vol/vol to sample buffer, Thermo Fisher Scientific, Cat# 39001), and β-mercaptoethanol (5%; vol/vol to sample buffer, Bio-Rad, Cat# 1610710) were loaded and separated on a 10% TGX Stain-Free polyacrylamide gel, followed by transferring onto polyvinylidene difluoride (PVDF) membranes. The blot was blocked by immersing in 5% non-fat milk containing TBST for 1 h at room temperature. The blots were probed for the following primary antibodies: Grp94 (1:1000; Thermo Fisher Scientific, Cat# 36-2600, RRID: AB_2533246), HSP90β (1:1000; Thermo Fisher Scientific, Cat# 37-9400, RRID: AB_2533349), or β-tubulin (1:1000; DSHB, Cat# E7-s, RRID: AB_528499) at 4°C overnight, followed by HRP-conjugated secondary antibodies (1:5000; Thermo Fisher Scientific, Cat# G-21040, RRID: AB_2536527; Cat# G-21234, RRID: AB_2536530) at room temperature for 1 h. Signals were visualized using Pierce enhanced chemiluminescence substrate (Thermo Fisher Scientific, Cat# 32106), and image acquisition was performed with Image Lab 6.0.1 (Bio-Rad) by ChemiDoc XRS+ System (Bio-Rad).

Electrophysiological Recordings

For cultures used for electrophysiological recordings, myotubes and spinal neurons were plated together on plain glass coverslips. Spontaneous synaptic currents (SSCs) were recorded from myoballs in 1-d old nerve-muscle co-culture by whole-cell patch clamp recording. The

cultures were perfused with the recording solution, containing 140 mM NaCl, 5 mM KCl, 1 mM $CaCl_2$, 1 mM $MgCl_2$, 10 mM HEPES, pH 7.4. Glass micropipettes (Sutter instrument) with 1-3 MΩ was filled with intra-pipette solution containing 145 mM KCl, 1 mM NaCl, 1 mM $MgCl_2$, 1 mM Mg-ATP, 10 mM HEPES, pH 7.2. Muscle cells were voltage clamped at –70 mV. All data were obtained using the MultiClamp 700B amplifier (Molecular Devices). The signals were filtered at 2 kHz and sampled at 20 kHz using Digidata 1440A (Molecular Devices, RRID: SCR_018455). The frequency of SSCs was defined as the number of events per second. The frequency, amplitude, rise time, decay time, and inter-event intervals of SSCs were analyzed using MiniAnalysis Program v6.0.3 (Synaptosoft, Inc., RRID: SCR_002184).

Fluorescence Microscopy

The fluorescent images were acquired on inverted epifluorescence microscopes (IX81 or IX83; Olympus) with an oil immersion 60X NA 1.42 objective lens or with an 20X NA 0.5 objective lens. Images were captured by iXon EMCCD camera (Andor) using the cell^R software (Olympus) on IX81, or by ORCA-Flash4.0 LT+ digital CMOS camera (Hamamatsu) using MicroManager software v.1.4 (Open Imaging, RRID: SCR_016865) on IX83. Quantitative measurements of fluorescence images were performed by ImageJ software (National Institute of Health, RRID: SCR_003070).

Fluorescence images of QD-labeled single AChR molecules were acquired on a super-resolution structured illumination microscopy (SR-SIM Elyra S1; Carl Zeiss) with an oil immersion 60X NA 1.4 objective lens. Images were obtained by a sCMOS camera (PCO Edge) with cooling system using ZEN 2.3 software (Carl Zeiss, RRID: SCR_018163).

Photobleaching of aneural AChR clusters was performed on a confocal microscope (LSM 800; Carl Zeiss) using 20X NA 0.8 objective lens and Diode laser line (488-nm or 561-nm) with 100% laser intensity. Identical settings were applied in all photobleaching experiments. A fluorescence image was taken immediately after photobleaching to ensure the complete photobleaching of AChR signals.

FRAP experiments were performed in total internal reflection fluorescence (TIRF) mode using Axio TIRF unit fitted on an inverted microscope equipped with oil immersion 100X NA 1.46 DIC objective lens. Photobleaching was performed by using Sapphire laser line (488 nm) with 50% laser intensity. Images were captured through Metamorph (Molecular Devices, RRID:

SCR_002368) by Evolve 512 EMCC camera (Photometrics). Identical settings were applied in all photobleaching experiments. To obtain the baseline of fluorescence intensity before photobleaching, 10 images at 1 s interval were taken in muscle cells expressing wild-type or mutant forms of GFP-XAC before photobleaching. After photobleaching, time-lapse images were taken at 1 s interval until the fluorescence intensity has reached the plateau level.

Statistical Analysis

All data from this study were collected from at least 3 replicates in independent experiments. Prism 7.0 (GraphPad) was used for statistical analyses. Detailed statistical results, including the exact *p* values, are provided in **Table 1**.

RESULTS

HSP90 expression and activity regulate AChR cluster formation and stability

As *Xenopus* primary cultures can be maintained in a range of different temperatures, this unique feature allows us to investigate whether temperature stress regulates NMJ development. Here, we incubated dissociated *Xenopus* myotomal tissues plated on coated substratum containing laminin under different culture temperatures (**Figure 1A**). At the normal culture temperature at 22°C (Peng et al., 1991), we detected an increasing percentage of cultured muscle cells with spontaneously formed aneural AChR clusters over the first 3 days in culture (**Figure 1B**). Interestingly, the formation of aneural AChR clusters was greatly reduced in muscle cultures incubated at lower temperatures (15°C or 10°C), which showed a temperature-dependent response during the entire 4-day culture period (**Figures 1A and 1B**). Notably, cultured muscle cells at lower temperatures did not show any obvious changes in the cytoskeletal organization, as evidenced by the integrity of microtubule networks throughout the cells across different temperature groups (**Figure 1A**). These data suggest that temperature stress causes a specific inhibition on aneural AChR cluster formation, rather than some non-specific cellular structure defects, in *Xenopus* muscle cultures.

The expression of HSP family of proteins could be induced in cells under stressful conditions, including temperature changes (Richter et al., 2010). A previous study showed that the molecular chaperone HSP90β plays a role in AChR cluster formation and maintenance by regulating rapsyn turnover (Luo et al., 2008), suggesting the involvement of stress proteins in regulating NMJ development. To examine if the expression of stress proteins in cultured *Xenopus* muscle cells is affected by low temperature treatment, we first performed quantitative real-time PCR to examine mRNA levels of several HSP90 family members in muscle cells incubated at different temperatures (**Figure 1C**). Surprisingly, the expression of HSP90α, the inducible isoform of HSP90, was not significantly changed in low temperature treatments. Instead, we detected a temperature-dependent increase in the expression of another two HSP90 family members, HSP90β and Grp94, in 10°C muscle cultures, which exhibited 2.5- and 5.2-fold increase in HSP90β and Grp94 mRNA levels, respectively, compared with that in 22°C muscle cultures. On the other hand, the expression level of mitochondrial-specific HSP90 protein TRAP-1 remained unchanged in different temperature groups. We then performed Western blot analyses to further investigate if the protein expressions of HSP90β and Grp94 are affected by

low temperature treatment (**Figures 1D and 1E**). Surprisingly, in contrast to the increase in HSP90β and Grp94 mRNA levels by temperature stress, the protein level of Grp94, but not HSP90β, was significantly reduced by 53.3 ± 0.06% in cultured muscle cells incubated at 10°C for 2 days (**Figure 1E**). These results suggested that temperature stress affects the expression of Grp94 that may regulate AChR clustering in cultured muscle cells.

To further investigate the regulation by HSP90 activity in aneural AChR clustering, we treated the cultured muscle cells with 17-AAG, a potent HSP90 inhibitor that alters the conformation of molecular chaperone machinery by inhibiting ATPase activity (Sharp and Workman, 2006). 17-AAG treatment exhibited a dose-dependent inhibition of aneural AChR cluster formation in cultured muscle cells (**Figure 1F**). In cultured cells treated with 0.25 nM 17-AAG, some aneural AChR clusters were found, but they showed a significant reduction in the fluorescence intensity and topological complexity of perforated aneural AChR clusters (**Figures 1G and 1H**), suggesting that HSP90 activity is involved in the formation and/or maintenance of topologically complex aneural AChR clusters. Taken together, these findings indicated that HSP90 expression and activity are precisely regulated at the optimal range in order to facilitate the formation of AChR clusters properly.

Previous studies showed that laminin-induced aneural AChR clusters in C2C12 myotubes can undergo topological transformation, mirroring the progressive morphological changes in synaptic AChR clusters at NMJs *in vivo* (Kummer et al., 2004; Lee et al., 2009). We next examined if HSP90 activity also participates in the topological remodeling of aneural AChR clusters. After identifying aneural AChR clusters in 2-d old muscle cultures, time-lapse imaging was then performed to monitor the dynamic changes in the morphology and intensity of the same AChR clusters in response to 1 nM 17-AAG treatment over 48 h. Specifically, pre-existing and newly inserted AChRs were differentially labeled by α-bungarotoxin conjugated with red and green fluorophores respectively, in accordance with a previously established protocol (Lee et al., 2009) and as illustrated in the schematic diagram (**Figure 1I**). By examining the pre-existing AChRs in control muscles, we observed a gradual dispersal of aneural AChR clusters, together with a reduction in AChR intensity, over a 48-h period (**Figures 1J and 1K**). However, such spontaneous dispersal of aneural AChR clusters was greatly inhibited in the presence of 17-AAG. In contrast, the intensity of newly inserted AChRs between control and 17-AAG-treated muscle cells showed no significant difference (**Figures 1J and 1L**). Interestingly, instead of dispersing

the entire aneural AChR clusters in control muscle cells, 17-AAG treatment caused a gradual loss of perforations, where podosome-like structures (PLSs) are located (Proszynski et al., 2009), within aneural AChR clusters (**Figure 1J**, bottom panels, arrows). Considering the involvement of PLSs in AChR endocytosis and topological remodeling of aneural AChR clusters in *Xenopus* primary muscle cultures and C2C12 myotubes (Lee et al., 2009; Proszynski et al., 2009; Yeo et al., 2015), we hypothesized that pharmacological inhibition of HSP90 activity affects the spatial localization of PLSs, leading to the stabilization of aneural AChR clusters. Collectively, our data demonstrated that HSP90 activity is involved in both the formation and topological remodeling/dispersal of aneural AChR clusters in cultured muscle cells.

The HSP90 chaperone machinery is known to be a crucial regulator in maintaining cellular homeostasis under stressful conditions and normal metabolism (Schopf et al., 2017). To rule out the possibility that pharmacological inhibition of HSP90 activity by 17-AAG causes global metabolic changes in cultured muscle cells, we firstly performed gas chromatography-mass spectrometry (GC-MS) analysis to compare the levels of various polar metabolites and fatty acids between control and 17-AAG-treated muscle cells. The principal component analyses (PCA) showed that these two experimental groups from the same biological sample overlapped in the first principal component of polar metabolites or fatty acids (**Figures 1-1A and 1-1C, Tables 1-1 and 1-2**). In addition, the heat map analyses also demonstrated a relatively similar amount of polar metabolites and fatty acids between control and 17-AAG-treated muscle cells from the same biological samples (**Figures 1-1B and 1-1D, Tables 1-1 and 1-2**). These results supported that 17-AAG treatment does not cause a significant change in the overall metabolite profile of cultured *Xenopus* muscle cells. Secondly, to eliminate the possible secondary effect of HSP90 inhibition on AChR clustering that is contributed by global changes in protein synthesis, we next used the OPP reagent, followed by click chemistry method to visualize the newly synthesized, nascent peptides/proteins (Liu et al., 2012; Slomnicki et al., 2016) (**Figure 1-1E**). We detected a similar level of OPP signals between control and 17-AAG-treated muscle cells (**Figure 1-1F**). In contrast, 25 μM cycloheximide (CHX), a well-known protein synthesis inhibitor, showed a significant reduction in OPP signals. Thirdly, to further validate the inhibitory effects on AChR clustering by 17-AAG are not due to defects in surface AChR insertion, we examined the density of single AChR molecules on the muscle surface using quantum dots as previously described (Geng et al., 2009) (**Figure 1-1G**). We detected a similar

density of surface AChR molecules between control and 17-AAG-treated muscle cells (**Figure 1-1H**), indicating that *de novo* synthesis, followed by surface targeting mechanisms, of AChR proteins are not affected by HSP90 inhibition. Taken together, we provided multiple lines of evidence supporting that HSP90 inhibition causes a specific effect on AChR clustering and remodeling, rather than a global change of different cellular events in cultured muscle cells.

Both diffuse and aneurally clustered AChRs contribute to the formation of synaptic AChR clusters

Prior to synaptogenesis, AChR molecules are present in the surface of muscle fibers (pre-existing AChRs) in the forms of aneurally clustered and diffuse receptors. It is believed that nerve innervation of skeletal muscles involves local signals to initiate synaptic AChR cluster formation and global signals to induce aneural AChR cluster dispersal (Dai and Peng, 1998). To demonstrate the differential contribution of aneurally clustered versus diffuse AChR molecules for the assembly of synaptic AChR clusters, laser-based photobleaching experiments were performed (**Figure 2**). Specifically, all surface AChRs (diffuse and aneurally clustered ones, referred to as old AChR) were first labeled with Rh-BTX. In the experimental groups, a high-power laser was used to photobleach the fluorescence signals of aneural AChR clusters, while diffuse AChRs in the entire muscle cells were unaffected. Latex beads coated with recombinant agrin were then added onto muscle cells, which has previously been shown to induce AChR clustering at the bead-muscle contacts in a spatially and temporally controllable manner (Lee et al., 2009). After 1- or 3-d agrin bead stimulation, newly synthesized and inserted AChRs (referred to as new AChR) were labeled with 488-BTX. In the experimental group with photobleaching of aneural AChR cluster before agrin bead stimulation, we detected 52.66 ± 0.05% reduction in the intensity of old AChR signals at 1-d agrin bead-muscle contacts, compared with the control group without photobleaching (**Figures 2A and 2B**). This result suggested that synaptic AChR clusters induced by agrin beads are recruited from both diffuse AChRs and aneural AChR clusters. Furthermore, the contribution of newly inserted AChRs to synaptic AChR clusters was negligible in the first day of agrin bead stimulation (**Figures 2A and 2C**). Different from previous observations in cultured C2C12 myotubes (Bruneau et al., 2008), our photobleaching approach however did not cause an effect similar to chromophore-assisted light inactivation (CALI) to induce dissipation of the illuminated aneural AChR clusters in

cultured *Xenopus* muscle cells labeled with either 594-BTX or Rh-BTX (**Figure 2-1**). Therefore, our results indicated the differential contribution of aneurally clustered and diffuse AChRs for the assembly of synaptic AChR clusters, rather than the secondary effects caused by photo-dissipation of illuminated AChR clusters and their associated scaffolding proteins.

To further examine whether HSP90 regulates the recruitment of both diffuse AChRs and aneural AChR clusters to the nascent postsynaptic sites, the same laser-based photobleaching experiment was performed using muscle cells pre-treated with 1 nM 17-AAG for 1 h before the experiment. A similar level of old AChR signals was detected at agrin bead-muscle contacts in 17-AAG-treated muscle cells either with or without photobleaching the aneural AChR clusters, suggesting that 17-AAG treatment abolishes the recruitment of aneural AChR clusters, not diffuse AChRs, to the synaptic sites (**Figures 2A and 2B**). On the other hand, the signals of new AChRs at agrin bead-muscle contacts showed no significant difference between control and 17-AAG-treated muscle cells (**Figures 2A and 2C**). As HSP90β plays a role in NMJ by regulating rapsyn localization and turnover (Luo et al., 2008), our immunostaining experiments further showed the association of rapsyn to those aneural AChR clusters that were stabilized by 17-AAG treatment in agrin bead-contacted muscles (**Figure 2-2**). In contrast, reduced rapsyn localization was detected at dispersing AChR clusters in control muscle cells after 4-8 hours agrin bead stimulation. Taken together, these data suggested that aneural AChR clusters and diffuse AChRs contribute equally to the assembly of synaptic AChR clusters, and the recruitment of aneural AChR clusters, but not diffuse or newly inserted AChRs, to agrin-induced synaptic clusters is dependent on HSP90 activity and rapsyn turnover.

Grp94 regulates ADF/cofilin-associated AChR redistribution upon agrin stimulation

To investigate if Grp94 is the HSP90 isoform that regulates aneural AChR cluster formation, we used antisense morpholino oligonucleotide (MO), which showed an effective knockdown of endogenous Grp94 expression level by Western blot analyses (**Figures 3A and 3B**). Grp94 knockdown caused a significant inhibition in the formation of aneural AChR clusters, including both bottom and top clusters (**Figure 3D**). Additionally, the intensity and complexity of aneural bottom AChR clusters were significantly reduced in Grp94 knockdown muscle cells (**Figures 3C and 3E**), in agreement with the observations in 17-AAG-treated muscles (**Figure 1G**). Given the known function of HSP90β in agrin-induced AChR cluster

formation and maintenance (Luo et al., 2008), we here showed that another HSP90 protein Grp94 is required for the initial formation of aneural AChR clusters.

A previous study demonstrated that ADF/cofilin localization is spatiotemporally correlated with AChR re-distribution from aneural to agrin-induced clusters (Lee et al., 2009). We next further studied whether Grp94 is required for ADF/cofilin-mediated AChR re-distribution. To test this, we performed dual-channel time-lapse imaging to monitor the change of AChR cluster morphology and intensity in correlation with ADF/cofilin localization at aneural AChR clusters in the same muscle cells before and after agrin bead stimulation (**Figures 3F-3I**). Consistent with previous studies (Lee et al., 2009), we also observed spatially localized GFP-XAC to be associated with agrin-induced AChR clusters at the bead-muscle contacts, which was accompanied with the reduction of localized GFP-XAC signals at the dispersing aneural AChR clusters, in muscle cells with GFP-XAC alone or with control MO + GFP-XAC. However, in Grp94 MO muscle cells, agrin-induced AChR clusters at the bead-contacted sites were significantly reduced, and the morphology and intensity of aneural AChR clusters remained largely unchanged before and after agrin bead stimulation (**Figures 3F-3I**). Importantly, the spatial localization of GFP-XAC associated with aneural and agrin-induced AChR clusters was largely reduced in Grp94 knockdown muscles (**Figures 3F, 3H, and 3I**). Taken together, our data suggested that Grp94 is required for the formation and dispersal of agrin-induced and aneural AChR clusters, respectively, possibly through modulating the spatial localization of ADF/cofilin.

Since ADF/cofilin is also considered as one of the PLS core markers to be associated with AChR clusters (Chan et al., 2020b), the reduced complexity of aneural AChR clusters in Grp94 knockdown muscle cells may be due to the dysregulation of PLS localization. To determine the requirement of Grp94 for the spatial localization of PLSs at aneural AChR clusters, our immunostaining experiments showed that XAC and p34-Arc, one of the Arp2/3 subunits, were spatially localized at the perforations of aneural AChR clusters in wild-type or control MO muscles, but not in Grp94 MO muscles (**Figures 3-1A-3-1C**). Likewise, PLS cortex marker vinculin was found to be localized at the edge of perforations within AChR clusters and at the cell periphery of wild-type or control MO muscles, but its spatial localization patterns were significantly reduced in Grp94 MO muscles (**Figures 3-1A and 3-1D**). These results suggested that MO-mediated knockdown of endogenous Grp94 may also affect proper localization of PLSs

553 at aneural AChR clusters, which in turn affect the stability of aneural AChR clusters and their
554 contribution to the synaptic clusters upon synaptogenic stimulation.
555
556 **Grp94 regulates spatial localization and dynamic turnover of ADF/cofilin at aneural AChR**
557 **clusters**
558 Since spatially localized ADF/cofilin may direct AChR endocytosis, trafficking, and/or
559 insertion for the assembly of synaptic AChR clusters at developing NMJs via transcytosis (Lee et
560 al., 2009; Yeo et al., 2015), we hypothesized that Grp94 activity regulates the dynamic turnover
561 of localized ADF/cofilin so as to control the stability of aneural AChR clusters. To test this, we
562 performed total internal reflection fluorescence (TIRF) imaging and fluorescence recovery after
563 photobleaching (FRAP) experiments on GFP-XAC-overexpressing muscle cells either with or
564 without 17-AAG treatment (**Figure 4**). Specifically, laser-based photobleaching was carried out
565 at the region of aneural AChR clusters (yellow rectangles in **Figure 4A**), followed by time-lapse
566 imaging to monitor the recovery of GFP-XAC fluorescence signals in the photobleached region
567 (**Figures 4A and 4B**). In control muscle cells, we detected a rapid recovery (in seconds after
568 photobleaching) of GFP-XAC signals at aneural AChR clusters. By examining the half-time of
569 fluorescence recovery (the time taken for the fluorescence intensity to recover to half of the
570 plateau level), we found that 17-AAG treatment caused a significant reduction in the recovery
571 half-time of GFP-XAC signals by 59% to 0.86 ± 0.2 s in the perforated regions of AChR clusters
572 (**Figure 4C**), indicating a much faster turnover rate of ADF/cofilin at aneural AChR clusters
573 upon HSP90 inhibition. Interestingly, we also detected a significant reduction in the recovery
574 half-time of GFP-XAC in the AChR-rich region of aneural clusters by 17-AAG treatment,
575 suggesting that HSP90 inhibition increases the turnover of perimembrane fraction of ADF/cofilin
576 at not only the perforated regions, but also the AChR-rich regions, of aneural clusters.
577 In migrating cells, HSP90 is known to form a molecular complex containing slingshot
578 (SSH), a serine/threonine phosphatase that dephosphorylates and activates ADF/cofilin, to
579 regulate lamellipodial protrusion and directed motility (Fotedar and Margolis, 2015), indicating
580 that HSP90 may modulate the phosphorylation state of ADF/cofilin. To test whether HSP90-
581 regulated ADF/cofilin turnover is mediated through phosphocycling, we performed TIRF-FRAP
582 experiments to compare the fluorescence recovery rate in muscle cells overexpressing different
583 phosphorylation mutant or wild-type forms of GFP-XAC (**Figure 4-1**). The constitutively active

(S3A) mutant of GFP-XAC exhibited a much slower recovery half-time than the wild-type form at both perforated and AChR-rich regions of aneural clusters, suggesting that active ADF/cofilin molecules bind to and modulate the dynamic turnover of actin filaments at both PLS and cell cortex at perforated and AChR-rich regions of AChR clusters, respectively. Similar to the effects of 17-AAG treatment (**Figure 4C**), the inactive ADF/cofilin mutant (S3E) showed a significant reduction in the recovery half time at both perforated and AChR-rich regions of aneural clusters, compared with the wild-type form. These data suggested that HSP90 may modulate ADF/cofilin activity via phosphorylation at its serine 3 residue.

Postsynaptic Grp94 regulates synaptic structure and function of developing NMJs

To examine the roles of postsynaptic Grp94 in the formation of NMJs *in vitro*, we examined nerve-induced AChR clustering in *Xenopus* nerve-muscle co-cultures by knocking down the endogenous expression of muscle Grp94 specifically. In wild-type nerve-muscle co-cultures (WT (M+N)) or in the chimeric co-cultures containing control MO muscles and WT neurons (Control MO (M) + WT (N)), nerve-induced synaptic AChR clusters were highly concentrated along the nerve-muscle contact sites (**Figure 5A**). In contrast, we observed a significant reduction in the percentage of nerve-muscle contacts with AChR clusters and the fluorescence intensity of nerve-induced AChR clusters in the chimeric co-cultures containing Grp94 MO muscles and WT neurons (Grp94 MO (M) + WT (N)) (**Figures 5A-5C**). These data suggested that Grp94 is required for the formation of nerve-induced AChR clusters, consistent with the requirement of Grp94 for agrin bead-induced AChR clustering as shown above (**Figure 3F**). To determine if pharmacological inhibition of HSP90 or molecular manipulation of Grp94 expression affects the spatial localization of rapsyn that leads to the reduced density of synaptic AChR clusters, we performed rapsyn immunostaining in nerve-muscle co-cultures treated with different HSP90 inhibitors or in different chimeric co-cultures (**Figure 5-1**). In wild-type (WT (M+N)) or in the chimeric co-cultures containing control MO muscles and WT neurons (Control MO (M) + WT (N)), rapsyn was spatially colocalized with nerve-induced synaptic AChR clusters (**Figure 5-1A**). However, significant reductions in AChR intensity and its associated rapsyn signals were detected in co-cultures treated with 17-AAG or PU-WS13, a specific Grp94 inhibitor. Similar observations were made in the chimeric co-cultures containing Grp94 MO muscles and WT neurons (Grp94 MO (M) + WT (N)) (**Figure 5-1**), indicating muscle Grp94

615 regulates the assembly of nerve-induced synaptic AChR clusters by modulating the precise
616 localization of postsynaptic scaffold protein rapsyn.
617 To further understand the role of HSP90 or Grp94 in AChR redistribution from aneural to
618 synaptic AChR clusters, we next examined the amount of internalized AChR vesicles at aneural
619 AChR clusters upon agrin bead stimulation in the presence of 17-AAG or PU-WS13 (**Figure 5-**
620 **2A**). Compared with control cells, HSP90 or Grp94 inhibition significantly reduced the number
621 of internalized AChR vesicles at aneural AChR clusters in agrin bead-contacted muscle cells
622 (**Figures 5-2A and 5-2B**). Taken together, our findings suggested that Grp94 is the specific
623 HSP90 family member that regulates the re-distribution and recruitment of aneural AChR
624 clusters to the postsynaptic specializations, likely through ADF/cofilin-mediated transcytosis
625 mechanism as previously proposed (Lee et al., 2009).
626 To determine the effects of postsynaptic Grp94 knockdown on synaptic functions of
627 developing NMJs, we performed whole-cell voltage-clamp recordings to examine the
628 spontaneous synaptic currents (SSCs) in 1-d old *Xenopus* nerve-muscle co-cultures (**Figure 5D**).
629 In the chimeric co-cultures of Grp94 MO (M) + WT (N), we detected a significant reduction in
630 the amplitude of SSCs (**Figures 5E and 5F**), which is likely attributed by the reduced AChR
631 density at the nerve-muscle contacts as observed in our cell imaging studies (**Figure 5A**). On the
632 other hand, we also detected a significant reduction in SSC frequency, leading to a right shift
633 pattern in the cumulative distribution of inter-event intervals (**Figures 5G and 5H**). In contrast,
634 postsynaptic Grp94 knockdown caused no significant effects on the rise time and decay time of
635 SSCs (**Figures 5I and 5J**), demonstrating that the channel properties of AChRs in muscles
636 remain unaffected. In summary, this study identified postsynaptic Grp94 as a novel regulator to
637 control the synaptic structures and functions at developing NMJs.

DISCUSSION

Temperature has long been considered as a physiological factor that affects neuronal growth and maintains synaptic homeostasis by modulating presynaptic and postsynaptic elements at the invertebrate NMJs (Tsai et al., 2012; Yeates et al., 2017; Zhu et al., 2018). South African clawed toad, *Xenopus laevis*, is an ectotherm vertebrate that has been widely used as an excellent animal model for embryology studies (Hobson, 1965). Since the body temperature of *Xenopus* is subjected to fluctuations in environmental temperature, this provides an ideal model for studying the molecular mechanisms underlying temperature-dependent alternations in the structure and functions of the vertebrate NMJs. In this study, we provided evidence showing that temperature-dependent alteration in Grp94 expression and activity regulates the recruitment of aneural AChR clusters for the assembly of postsynaptic specializations through modulating ADF/cofilin activity, suggesting a novel role of Grp94 in the formation of vertebrate NMJs. Consistent with a previous study showing the function of cytosolic HSP90 member, HSP90β, for regulating rapsyn turnover and agrin-induced AChR cluster formation (Luo et al., 2008), our present study further identified another HSP90 family member Grp94, an ER-resident molecular chaperone, in regulating AChR clustering and remodeling during NMJ development.

HSP90 proteins are implicated in diverse biological processes, in which a variety of coordinated regulatory mechanisms are involved to control their expression and activity (Prodromou, 2016). In response to stressful conditions, heat shock factor 1 is an important regulator responsible for the transcriptional regulation of HSP90 genes. In this study, mRNA levels of HSP90β and Grp94 were upregulated in cultured *Xenopus* muscle cells by low temperature treatment (**Figure 1C**). However, Grp94 protein level was found to be significantly reduced under low temperature stress (**Figures 1D and 1E**). This discrepancy between mRNA and protein levels of Grp94 could be explained by a negative feedback mechanism (DiDomenico et al., 1982; Bader et al., 2015), in which Grp94 mRNA may be upregulated in order to compensate a reduced amount of Grp94 protein level. As both temperature stress and HSP90 inhibitor significantly suppress the formation of aneural AChR clusters, this suggests that HSP90 expression and activity are essential for the regulation of AChR clustering in cultured muscle cells.

One common concern with all HSP90 studies is that pharmacological inhibition of HSP90 activity may be causing non-specific, global changes in cell metabolism and protein

669 expression. Here, we employed multiple experimental approaches to show that it is unlikely the
670 case in the present study: targeted metabolomics (polar metabolites and fatty acids) study
671 (**Figures 1-1A-1-1D**), nascent protein synthesis assay (**Figures 1-1E and 1-1F**), single AChR
672 molecule labeling (**Figures 1-1G and 1-1H**), and newly inserted AChR labeling **(Figure 2C)**.
673 Together, results from all these experiments indicated that HSP90 inhibition by 17-AAG causes
674 a specific effect on AChR clustering and remodeling, rather than a plethora of changes in
675 different cellular events.
676 Previous genetic studies demonstrated that nerve-independent formation of AChR pre-
677 patterns can be detected in the central region of muscle fibers at developing NMJs *in vivo* (Yang
678 et al., 2000; Lin et al., 2001; Yang et al., 2001). Similarly, spontaneously formed aneural AChR
679 clusters can be found in cultured muscle cells, suggesting muscle-intrinsic mechanisms
680 underlying initial AChR cluster formation. Upon synaptogenic induction, it is hypothesized that
681 the dispersal of aneural AChR clusters is temporally coupled with the formation of synaptic
682 AChR clusters (Dai and Peng, 1998). A previous study performed by single AChR tracking
683 approach showed the contribution of surface AChR molecules, derived from either aneural
684 clusters or diffuse receptor pool, to the sites of nerve-muscle contacts (Geng et al., 2009).
685 Interestingly, a recent study further provided a definite evidence to demonstrate the recruitment
686 of aneural AChR clusters for the assembly of nerve-induced synaptic AChR clusters (Chan et al.,
687 2020b). Consistent with that, our present study confirmed the differential contribution of pre-
688 existing AChRs (from aneural clusters and diffuse AChRs) versus newly synthesized and
689 inserted AChRs for the assembly of agrin-induced postsynaptic specializations (**Figure 2**), in
690 which HSP90 or Grp94 is required for the recruitment of AChRs from aneural clusters, but not
691 from diffuse nor newly inserted ones. The stability of AChR clusters is known to be regulated
692 by rapsyn, a multi-domain synaptic adaptor protein for AChR anchoring by interacting directly
693 with actin or indirectly with various cytoskeletal regulatory proteins (Wang et al., 1999; Oury et
694 al., 2019; Xing et al., 2020). Apart from serving as a scaffolding molecule at NMJs, rapsyn
695 contains E3 ligase activity that increases neddylation of AChR subunits (Li et al., 2016), leading
696 to the stabilization of AChR clusters. Consistent with this notion, we observed the association of
697 rapsyn with aneural AChR clusters that are stabilized by HSP90 inhibition (**Figure 2-2**),
698 preventing AChR molecules of aneural clusters from being recruited to the synaptic sites.

It is worth noting that our laser-based photobleaching experiments did not cause photo-dissipation of illuminated AChR clusters and their intracellular scaffolding proteins (**Figure 2-1**), as previously observed in cultured C2C12 myotubes (Bruneau et al., 2008). Although the exact molecular mechanism underlying photo-dissipation of AChR clusters remains unknown, illumination of a photosensitiser chromophore (e.g. Alexa Fluor 594) may generate reactive oxygen species, leading to limited damage of surrounding target proteins through CALI. In early *Xenopus* embryos, there are various genetically regulated enzymes involved in antioxidant defences (Rizzo et al., 2007). These enzymes may dampen the possible effects of photo-dissipation in cultured *Xenopus* muscle cells. Therefore, our experimental approach allows us to study the essential roles of AChR molecules derived from dispersing aneural AChR clusters, rather than the destruction and removal of illuminated AChR clusters and their associated scaffolding proteins, in the assembly of agrin-induced synaptic AChR clusters.

PLS is composed of a core domain containing F-actin and its associated proteins such as ADF/cofilin, Arp2/3 complex, and cortactin, as well as a cortex domain containing focal adhesion proteins such as talin, vinculin, and paxillin. Apart from actin-binding proteins, a recent study also showed that a microtubule-binding protein, microtubule-actin cross linking factor 1 (Macf1), is concentrated at PLS within AChR clusters (Oury et al., 2019). Among different PLS proteins, ADF/cofilin is known to regulate AChR endocytosis, trafficking, and/or insertion at developing NMJs (Lee et al., 2009; Yeo et al., 2015). The actin-binding activity of ADF/cofilin is tightly controlled by a balancing act of phosphorylation and dephosphorylation on its serine-3 residue by LIM or testicular (TES) kinases and SSH phosphatase, respectively. Active, non-phosphorylated ADF/cofilin mediates actin depolymerization by binding to and severing F-actin, while serine-3 phosphorylated ADF/cofilin inhibits its binding to G-actin and F-actin (Bernstein and Bamburg, 2010). As a previous study indicated, constitutively active (S3A) mutant of GFP-XAC is highly localized at the perforated regions of aneural AChR clusters compared with inactive (S3E) mutant or wild-type forms of GFP-XAC (Lee et al., 2009), suggesting that active ADF/cofilin molecules are preferentially localized at perforated regions of AChR clusters to spatially modulate actin dynamics. Surprisingly, we found that 17-AAG treatment caused a significant increase in the turnover rate of GFP-XAC at both perforated and AChR-rich regions of aneural clusters (**Figure 4**), suggesting that ADF/cofilin modulates actin dynamics at not only the PLS, but also the cell cortex in association with AChR molecules.

Cortical actin filaments are organized as a dense meshwork that lies directly underneath the plasma membrane (Chugh and Paluch, 2018), where ADF/cofilin-mediated dynamics of cortical actin filaments may facilitate endocytosis and exocytosis events in vesicular trafficking of AChR molecules (Lee et al., 2009; Lee et al., 2014). Similar to the effects of HSP90 inhibition, we observed an increased turnover rate in muscle cells expressing phospho-mimic inactive S3E mutant of GFP-XAC (**Figure 4-1**), suggesting that HSP90 inhibition may promote phosphorylation or suppress dephosphorylation of ADF/cofilin at perforated and AChR-rich regions of aneural clusters. The phosphorylated ADF/cofilin is inactive in actin binding, therefore it is incapable of modulating the dynamics of both cortical actin (for mobilizing AChR molecules) and PLS actin (for directing vesicular trafficking of AChR molecules) at aneural clusters (**Figure 6**).

As HSP90 is known to form a molecular complex containing SSH in migrating cells (Fotedar and Margolis, 2015), HSP90 may indirectly modulate the phosphorylation state and turnover rate of ADF/cofilin in cultured muscle cells. Apart from the phosphorylation regulation, a recent study has identified that cofilin is a physiologically relevant neddylation target that modulates cytoskeletal actin dynamics in neuronal outgrowth (Vogl et al., 2020). Since rapsyn contains E3 ligase activity (Li et al., 2016), it would be of interest to determine if rapsyn regulates the dynamic turnover of ADF/cofilin via neddylation at AChR clusters. In addition, the spatial localization of ADF/cofilin at the postsynaptic sites can also be regulated by 14-3-3ζ (Lee et al., 2009). As ER stress inducers are known to modulate the expression levels of 14-3-3ζ and Grp94 in hippocampal neurons (Murphy et al., 2008; Brennan et al., 2013), whether temperature stress-induced alterations in Grp94 expression and activity affect 14-3-3ζ-regulated ADF/cofilin localization at AChR clusters remain to be examined. Taken together, we speculate that Grp94 inhibition or knockdown may affect either the dynamic turnover (via phosphocycling and/or neddylation) or the spatial localization (via 14-3-3ζ) of ADF/cofilin, which in turn controls actin-mediated vesicular trafficking of AChRs in the formation of NMJs. Future studies will be focused on elucidating the detailed molecular mechanisms underlying how Grp94 regulates the upstream regulators of ADF/cofilin activity and localization in aneural versus synaptic AChR clusters at developing NMJs.

In the electrophysiological recordings, we showed a significant reduction of SSC frequency in the chimeric co-cultures of Grp94 knockdown muscles and wild-type neurons

(**Figure 5G**). This effect may be attributed by the reduced probability of neurotransmitter release, suggesting that postsynaptic Grp94 may also be involved in retrograde signaling to affect presynaptic functions. As Grp94 is one of the major Ca^{2+} binding proteins at the ER (Van et al., 1989), it has to contend during the fluctuations in free Ca^{2+} in the lumen, as protein-bound Ca^{2+} is released through the ER membrane channels to the cytosol in response to the physiological demands of the cell (Marzec et al., 2012). Previous studies identified that the activity of Ca^{2+}/calmodulin-dependent protein kinase II (CaMKII) in postsynaptic muscles retrogradely modulates the neurotransmitter release at Drosophila NMJs (Haghighi et al., 2003). Additionally, conditional deletion of Grp94 results in the loss of β-catenin signaling in the intestinal epithelium (Liu et al., 2013). While muscle β-catenin is known to retrogradely regulate presynaptic differentiation or function at NMJs (Li et al., 2008), it will be of interest to investigate whether postsynaptic Grp94 serves as a regulator of CaMKII- or β-catenin-mediated retrograde signaling to affect presynaptic structure and function.

In summary, this study provides the first evidence suggesting that temperature stress regulates the development of vertebrate NMJs through the expression and activity of postsynaptic Grp94. It is important to note that auto-antibodies against Grp94 has recently been identified in myasthenia gravis (MG), an autoimmune NMJ disease (Suzuki et al., 2011). Another recent study has also shown a significant positive correlation between the age of MG onset and the expression level of Grp78, another ER chaperone (Iwasa et al., 2014). Therefore, results of our study provide insights into not only the fundamental mechanisms underlying the vertebrate NMJ development, but also the pathogenic mechanisms underlying ER stress response and NMJ disruption in MG.

FIGURE LEGENDS

Figure 1. Temperature Stress-Modulated Expression and Pharmacological Inhibition of HSP90 Regulate the Formation and Stability of Aneural AChR Clusters

(A) Representative images showing the inhibition of aneural AChR cluster formation in cultured *Xenopus* muscle cells treated with lower temperatures. Tubulin immunostaining indicated that cytoskeletal structures were largely unaffected in muscle cells cultured at different temperatures, ranging from 10 to 22^{o}C.

(B) Quantification showing the percentage of cultured muscle cells with bottom aneural AChR clusters at different culturing temperatures over 4 days. n = 150 cells in each condition from 3 independent experiments.

(C) Quantification showing the relative mRNA levels of HSP90α, HSP90β, Grp94, and TRAP-1 in 2-d old *Xenopus* muscle cells cultured at different temperatures. n = 3 independent experiments.

(D and E) Western blot analysis (D) and quantification (E) showing the protein expression level of HSP90β and Grp94 in *Xenopus* muscle cells cultured at 22°C or 10°C for 2 days. β-tubulin was used as the loading control for normalization.

(F) Quantification showing the dose-dependent effects of 17-AAG on aneural AChR cluster formation in cultured *Xenopus* muscle cells. n = 191 (Control), 198 (0.25 nM 17-AAG), 199 (0.5 nM 17-AAG), and 200 (1 nM 17-AAG) muscle cells from 4 independent experiments.

(G) Representative images showing the organization and intensity of aneural AChR clusters in response to 17-AAG treatment. 8-bit pseudo-color images highlight the relative fluorescence intensity of AChR clusters in different conditions.

(H) Quantification showing the effects of 17-AAG on the intensity and complexity of aneural AChR clusters. n = 55 (Control) and 44 (17-AAG) muscle cells from 3 independent experiments for fluorescence intensity measurement (left y-axis). n = 76 (Control) and 48 (17-AAG) muscle cells from 4 independent experiments for cluster complexity measurement (right y-axis).

(I) Schematic diagram illustrating the differential labeling procedure to identify pre-existing (red) and newly inserted (green) AChRs with α-bungarotoxin conjugated with different fluorophores.

(J) Representative sets of time-lapse images showing the topological changes and fluorescence intensity of pre-existing (left panels) and newly inserted (right panels) AChRs at aneural clusters in control (top panels) or 17-AAG-treated (bottom panels) muscle cells. Arrows indicate the progressive reduction of perforated area in aneural AChR clusters. 8-bit pseudo-color images highlight the change in the fluorescence intensity of the same aneural AChR clusters over 48 hours with or without 17-AAG treatment.

(K and L) Individual value plots showing the percentage change in the fluorescence intensity of pre-existing (K) and newly inserted (L) AChRs in the same aneural AChR clusters at different time-points between control and 17-AAG-treated cells. n = 46 (Control) and 41 (17-AAG) muscle cells from 3 independent experiments.

Scale bars represent 10 μm. Data are shown as mean ± SEM (B, C, E, F, and H) or ± SD (K and L). Two-way ANOVA with Tukey's multiple comparisons test (B and C), student's t-test (E and H), one-way ANOVA with Tukey's multiple comparison test (F), and two-way ANOVA with

Sidak's multiple comparisons test (K and L). *, **, **** represent $p \leq 0.05$, 0.01, and 0.0001 respectively. n.s.: non-significant.

Extended Data: Figure 1-1. HSP90 Inhibition Does Not Cause Non-Specific, Global Changes in Cell Metabolism and Protein Expression in Cultured Muscle Cells

(A and B) Principal component analysis (A) and heat map comparison (B) showing a panel of different polar metabolites between control and 17-AAG-treated cultured *Xenopus* muscle cells. Control (green circles) and 17-AAG-treated (red circles) samples were not clearly distinguished in the first principal component axis (x-axis). n = 3 biological samples. p-values of each polar metabolite examined were shown in Table 1-1.

(C and D) Principal component analysis (C) and heat map comparison (D) showing a panel of different fatty acids between control and 17-AAG-treated cultured *Xenopus* muscle cells. Control (green circles) and 17-AAG-treated (red circles) samples were not clearly distinguished in the first principal component axis (x-axis). n = 3 biological samples. p-values of each fatty acid examined were shown in Table 1-2.

(E) Representative images showing no significant change in the amount of nascent peptides/proteins between control and 17-AAG-treated muscle cells, as shown by OPP signals.

(F) Quantification showing the fluorescence intensity of OPP signals in muscle cells at different experimental groups. n = 237 (control), 245 (CHX), and 251 (17-AAG) muscle cells from 3 independent experiments.

(G) Representative images showing a similar density of quantum dot-labeled single AChR molecules in membrane surface between control and 17-AAG-treated muscle cells.

(H) Quantification showing the number of single AChR molecules in membrane surface per unit area between control and 17-AAG-treated muscle cells. n = 42 (control) and 33 (17-AAG) muscle cells from 3 independent experiments.

Scale bars represent 100 μm (E) or 10 μm (G). Data are shown as mean ± SEM (F) or ± SD (H). One-way ANOVA with Dunnett's multiple comparisons test (F) and Student's t-test (H). * represents $p \leq 0.05$. n.s.: non-significant.

Extended Data: Table 1-1. A list of p-values in comparing the relative amount of polar metabolites between control and 17-AAG-treated muscle cells.

Extended Data: Table 1-2. A list of p-values in comparing the relative amount of fatty acids between control and 17-AAG-treated muscle cells.

Figure 2. HSP90 Regulates AChR Recruitment from Aneural Clusters to Agrin-Induced Clusters

(A) Representative images showing the differential contribution of diffuse and aneurally clustered AChRs to agrin bead-induced synaptic AChR clusters in control or 17-AAG-treated muscle cells using laser-based photobleaching approach. Green boxes indicate the magnified view of muscle cells with agrin bead contacts at different time-points for clarity. Yellow dotted-line boxes indicate the photobleaching region of aneural AChR clusters before agrin bead

stimulation. Dotted lines highlight the periphery of muscle cells. 8-bit pseudo-color images highlight the relative fluorescence intensity of pre-existing (old AChR) and newly inserted (new AChR) AChR signals in muscle cells contacted by agrin beads for 1 and 3 days.

(B and C) Quantification showing the fluorescence intensity of pre-existing (B) and newly inserted (C) AChR signals at agrin bead-muscle contacts in control or 17-AAG-treated muscle cells, either with or without photobleaching of aneural AChR clusters before agrin bead stimulation. n = 11 (control, without photobleaching), 16 (control, photobleaching of aneural AChR clusters), 17 (17-AAG-treated, without photobleaching), and 21 (17-AAG-treated, photobleaching of aneural AChR clusters) muscle cells from 3 independent experiments.

Scale bars represent 10 μm. Data are shown as mean ± SEM. Two-way ANOVA with Tukey's multiple comparisons test. * and ** represent $p \leq 0.05$ and 0.01 respectively. n.s.: non-significant.

Extended Data: Figure 2-1. No Photo-Dissipation of Illuminated Aneural AChR Clusters Was Observed in Cultured *Xenopus* Muscle Cells Labeled with Alexa Fluor 594-Conjugated α-Bungarotoxin

Representative images showing no photo-dissipation effects on illuminated aneural AChR clusters in cultured *Xenopus* muscle cells labeled with either rhodamine-α-bungarotoxin (Rh-BTX) (left panels) or Alexa Fluor 594-BTX (594-BTX) (right panels). Newly synthesized and inserted AChRs were labeled with Alexa Fluor 488-BTX (488-BTX) at 6 and 24 h after photobleaching. Yellow boxes indicate the photobleaching region covering the entire aneural AChR clusters, while the yellow dotted line box indicates the photobleaching region covering a part of aneural AChR clusters. The recovery of either Rh-BTX or 594-BTX signals was observed at 6-h and 24-h after photobleaching the entire (arrows) or partial (arrowheads) region of AChR clusters, respectively.

Scale bar represents 10 μm.

Extended Data: Figure 2-2. HSP90 Inhibition Stabilizes Aneural AChR Clusters and Their Associated Rapsyn Localization

Representative images showing the stabilization of rapsyn-associated aneural AChR clusters (left panels) and the inhibition of agrin bead-induced synaptic AChR cluster formation (right panels) by 17-AAG treatment. After 4-8 h agrin bead stimulation, reduced rapsyn signals were detected at dispersing AChR clusters in control muscle cells. In contrast, rapsyn was highly localized at stabilized aneural AChR clusters in 17-AAG-treated muscle cells. At the agrin bead-muscle contacts, agrin-induced AChR clusters were associated with rapsyn localization in control muscle cells, but not in 17-AAG-treated muscle cells.

Scale bars represent 5 μm.

Figure 3. Grp94 Knockdown Inhibits Agrin Bead-Induced AChR Clustering by Modulating ADF/Cofilin Localization

(A and B) Western blot analysis (A) and quantification (B) showing the expression level of Grp94 in wild-type (WT), control MO, and Grp94 MO embryos. β-tubulin was used as the loading control for normalization.

(C) Representative images showing the intensity and complexity of aneural AChR clusters in response to Grp94 knockdown. 8-bit pseudo-color images highlight the relative fluorescence intensity of AChR clusters in control versus Grp94 knockdown muscle cells. Insets show the fluorescent dextran signals, indicating the presence of MO.

(D) Quantification showing the effects of MO-mediated Grp94 knockdown on the formation of aneural AChR clusters in cultured muscles. n = 150 (WT), 143 (Control MO), and 150 (Grp94 MO) muscle cells from 3 independent experiments.

(E) Quantification showing the effects of MO-mediated Grp94 knockdown on the intensity and complexity of aneural AChR clusters. n = 64 (WT), 47 (Control MO), and 52 (Grp94 MO) muscle cells from 4 independent experiments for fluorescence intensity measurement (left y-axis). n = 44 (WT), 42 (Control MO), and 44 (Grp94 MO) muscle cells from 4 independent experiments for cluster complexity measurement (right y-axis).

(F) Representative sets of time-lapse images showing the effects of Grp94 knockdown on GFP-XAC localization in association with the dispersal of aneural AChR clusters (left panels) and with the formation of agrin bead-induced AChR clusters (right panels). 8-bit pseudo-color images highlight the change in fluorescence intensity of aneural AChR clusters after agrin bead stimulation for 4 hours.

(G and H) Individual value plots showing the percentage change in the fluorescence intensities of AChRs (G) and GFP-XAC (H) in the same aneural AChR clusters among different conditions after agrin bead stimulation for 4 hours. n = 12 (GFP-XAC alone), 9 (Control MO + GFP-XAC), and 11 (Grp94 MO + GFP-XAC) muscle cells from 3 independent experiments.

(I) Quantification showing the effects of Grp94 knockdown on agrin bead-induced AChR clustering (left y-axis) and GFP-XAC localization (right y-axis). n = 24 (GFP-XAC alone), 24 (Control MO + GFP-XAC), and 21 (Grp94 MO + GFP-XAC) muscle cells from 4 independent experiments.

Scale bars represent 5 μm. Data are shown as mean ± SEM (B, D, E and I) or ± SD (G and H). One-way ANOVA with Dunnett's multiple comparisons test (B and E), two-way ANOVA with Tukey's multiple comparisons test (D), two-way ANOVA with Sidak's multiple comparison test (G and H) and one-way ANOVA with Turkey's multiple comparison test (I). *, **, ***, **** represent $p \leq 0.05$, 0.01, 0.001, and 0.0001 respectively. n.s.: non-significant.

<u>Extended Data:</u> Figure 3-1. Grp94 Knockdown Affects PLS Localization at Aneural AChR Clusters

(A) Representative images showing the effects of Grp94 knockdown on the spatial localization of PLS core markers (*Xenopus* ADF/cofilin (XAC) and p34-Arc) and cortex marker (vinculin) at aneural AChR clusters.

(B) Quantification showing the spatial enrichment of XAC at aneural AChR cluster versus non-AChR regions in the same muscle cells. n = 44 (WT), 43 (Control MO), and 38 (Grp94 MO) muscle cells from 4 independent experiments.

(C) Quantification showing the spatial enrichment of p34-Arc at aneural AChR cluster versus non-AChR regions in the same muscle cells. n = 27 (WT), 29 (Control MO), and 32 (Grp94 MO) muscle cells from 3 independent experiments.

(D) Quantification showing the spatial enrichment of vinculin at aneural AChR cluster versus non-AChR regions in the same muscle cells. n = 39 (WT), 33 (Control MO), and 33 (Grp94 MO) muscle cells from 3 independent experiments.

Scale bars represent 10 μm. Data are shown as mean ± SEM. One-way ANOVA with Dunnett's multiple comparisons test. *, ** represent $p \leq 0.05$ and 0.01 respectively.

Figure 4. HSP90 Inhibition Accelerates ADF/Cofilin Turnover at Different Regions of Aneural AChR Clusters

(A) Representative time-lapse TIRF images showing the fluorescence recovery of GFP-XAC signals after photobleaching the region of aneural AChR clusters (yellow rectangles, which are magnified in bottom rows with multiple timepoints) in control or 17-AAG-treated muscle cells. 8-bit pseudo-color images highlight the relative fluorescence intensity of GFP-XAC signals.

(B and C) Quantification showing the FRAP curves (B) and the calculated recovery half time (C) of GFP-XAC signals at perforated and AChR-rich regions within aneural AChR clusters in control versus 17-AAG-treated muscle cells. n = 12 (Control) and 7 (17-AAG) muscle cells from 3 independent experiments.

Scale bars represent 5 μm. Data are shown as mean ± SEM. Student's t-test. *, ** represent $p \leq 0.05$ and 0.01 respectively.

<u>Extended Data:</u> Figure 4-1. ADF/Cofilin Phosphorylation Mutants Exhibit Differential Turnover Rates at Aneural AChR Clusters

(A and B) Quantification showing the FRAP curves of GFP-XAC signals at perforated (A) and AChR-rich (B) regions within aneural AChR clusters in cultured muscle cells over-expressing wild-type or serine-3 phosphorylation mutant forms (S3A and S3E) of GFP-XAC. n = 13 (GFP-XAC), 8 (GFP-XAC(S3A)), and 12 (GFP-XAC(S3E)) muscle cells from 3 independent experiments.

(C) Quantification showing the calculated recovery half time of GFP-XAC signals at perforated and AChR-rich regions within aneural AChR clusters in cultured muscle cells over-expressing wild-type or serine-3 phosphorylation mutant forms of GFP-XAC. n = 13 (GFP-XAC), 8 (GFP-XAC(S3A)), and 12 (GFP-XAC(S3E)) muscle cells from 3 independent experiments.

Data are shown as mean ± SEM. One-way ANOVA with Tukey's multiple comparisons test. *, ** represent $p \leq 0.05$ and 0.01 respectively. n.s.: non-significant.

Figure 5. Postsynaptic Grp94 Knockdown Impairs Synaptic Structures and Functions at Developing NMJs

(A) Representative images showing the effects of muscle Grp94 knockdown on nerve-induced AChR clustering. Fluorescent dextran signals indicate the presence of MO. Arrows indicate sites of nerve-muscle contacts.

(B and C) Quantification showing the effects of muscle Grp94 knockdown on the percentage of nerve-muscle contacts with AChR clusters (B) and the fluorescence intensity of nerve-induced AChR clusters (C) in 1-d old *Xenopus* nerve-muscle co-cultures. n = 150 (wild-type (WT)), 146 (Control MO), and 191 (Grp94 MO) nerve-muscle contacts from 3 independent experiments for quantifying the percentage of nerve-muscle contacts with synaptic AChR clusters (B). n = 33 (WT), 31 (Control MO), and 33 (Grp94 MO) nerve-muscle contacts from 3 independent experiments for measuring AChR fluorescence intensity (C).

(D) Representative images showing the whole-cell patch-clamp recording on a Grp94 MO muscle cell innervated by a WT spinal neuron. Fluorescent dextran signals indicate the presence of MO.

(E) Representative electrophysiological recording traces of SSCs recorded from WT, control MO, or Grp94 MO muscles that were innervated by WT spinal neurons.

(F and G) Quantification showing the effects of muscle Grp94 knockdown on the amplitude (F) and frequency (G) of SSCs. n = 10 (WT), 9 (Control MO), and 9 (Grp94 MO) nerve-muscle pairs from 3 independent experiments.

(H-J) Cumulative distribution plots of the inter-event interval (H), 10–90% rise time (I), and decay time (J) of SSCs recorded from WT, Control MO, or Grp94 MO muscles innervated by WT spinal neurons. n = 10 (WT), 9 (Control MO), and 9 (Grp94 MO) nerve-muscle pairs from 3 independent experiments.

Scale bars represent 10 μm. "M": muscle; "N": neuron. Data are represented as mean ± SEM (B and C) and mean ± SD (F and G). One-way ANOVA with Tukey's multiple comparisons test (B and C). Kruskal–Wallis ANOVA test with Dunn's multiple comparison test (F and G). *, *** represent $p \leq 0.05$ and 0.001, respectively.

Extended Data: Figure 5-1. HSP90 Inhibition or Grp94 Knockdown Suppresses Nerve-Induced Synaptic AChR Clusters with Reduced Rapsyn Localization

(A) Representative images showing the effects of HSP90 inhibition or muscle Grp94 knockdown on nerve-induced AChR clustering and rapsyn localization at nerve-muscle contact sites. Dotted lines indicate nerve-muscle contacts. Insets show fluorescent dextran signals as cell-lineage tracer. "M": muscle; "N": neuron.

(B and C) Quantifications showing the fluorescence intensity of synaptic AChR clusters (B) and rapsyn (C) along the nerve-muscle contacts in 1-d old *Xenopus* nerve-muscle co-cultures in the presence or absence of 17-AAG or PU-WS13 and in the chimeric co-cultures of wild-type neurons and muscle cells with control MO or Grp94 MO. n = 26 (Control), 9 (17-AAG), 10 (PU-WS13), 18 (Control MO), and 14 (Grp94 MO) from 4 independent experiments.

Scale bar represents 10 μm. Data are shown as mean ± SEM. One-way ANOVA with Dunnett's multiple comparisons test. *, **, *** represent $p \leq 0.05$, 0.01 and 0.001 respectively. n.s.: non-significant.

Extended Data: Figure 5-2. Grp94 Inhibition Reduces The Amount of AChR Vesicles at Aneural Clusters in Agrin-Stimulated Muscle Cells

(A) Representative images showing the effects of 17-AAG or PU-WS13 on AChR internalization at aneural clusters upon agrin stimulation. Images of aneural AChR clusters were taken from a single focal plane (surface AChR), while the maximal projection of intracellular AChR signals was constructed of a stack of 11 images at 0.2 μm per frame (internal AChR).

(B) Quantification showing the effects of 17-AAG or PU-WS13 on AChR internalization at aneural clusters upon agrin stimulation for 0.5 or 4 h. n = 27 (Control, 0.5 h), 28 (17-AAG, 0.5 h), 23 (PU-WS13, 0.5 h), 19 (Control, 4 h), 28 (17-AAG, 4 h), and 29 (PU-WS13, 4 h) muscle cells from 3 independent experiments.

Scale bar represents 5 μm. Data are shown as mean ± SD. One-way ANOVA with Dunnett's multiple comparisons test. *, **** represent $p \leq 0.05$ and 0.0001 respectively.

Figure 6. Temperature Stress-Induced Grp94 Inhibition Affects AChR Recruitment from Aneural to Synaptic Clusters by Modulating ADF/Cofilin Phosphorylation and Activity

To allow AChR redistribution during neuromuscular synaptogenesis, modulation of actin dynamics at the cell cortex and at the PLS are required for mobilizing AChR molecules and facilitating vesicular trafficking of AChR molecules at aneural clusters, respectively. Our findings suggest that temperature stress-induced Grp94 inhibition promotes phosphorylation or suppress dephosphorylation of ADF/cofilin at perforated and AChR-rich regions of aneural clusters, thereby stabilizing them against agrin-induced dispersal and recruitment to the postsynaptic sites.

REFERENCES

Bader DM, Wilkening S, Lin G, Tekkedil MM, Dietrich K, Steinmetz LM, Gagneur J (2015) Negative feedback buffers effects of regulatory variants. Mol Syst Biol 11:785.

Bernstein BW, Bamburg JR (2010) ADF/cofilin: a functional node in cell biology. Trends Cell Biol 20:187-195.

Borges LS, Ferns M (2001) Agrin-induced phosphorylation of the acetylcholine receptor regulates cytoskeletal anchoring and clustering. J Cell Biol 153:1-12.

Brennan GP, Jimenez-Mateos EM, McKiernan RC, Engel T, Tzivion G, Henshall DC (2013) Transgenic overexpression of 14-3-3 zeta protects hippocampus against endoplasmic reticulum stress and status epilepticus in vivo. PLoS One 8:e54491.

Bruneau EG, Brenner DS, Kuwada JY, Akaaboune M (2008) Acetylcholine receptor clustering is required for the accumulation and maintenance of scaffolding proteins. Curr Biol 18:109-115.

Chan ZC, Oentaryo MJ, Lee CW (2020a) MMP-mediated modulation of ECM environment during axonal growth and NMJ development. Neurosci Lett:134822.

Chan ZC, Kwan HR, Wong YS, Jiang Z, Zhou Z, Tam KW, Chan YS, Chan CB, Lee CW (2020b) Site-directed MT1-MMP trafficking and surface insertion regulate AChR clustering and remodeling at developing NMJs. Elife 9.

Chong J, Wishart DS, Xia J (2019) Using MetaboAnalyst 4.0 for Comprehensive and Integrative Metabolomics Data Analysis. Curr Protoc Bioinformatics 68:e86.

Chugh P, Paluch EK (2018) The actin cortex at a glance. J Cell Sci 131.

Csermely P, Schnaider T, Soti C, Prohaszka Z, Nardai G (1998) The 90-kDa molecular chaperone family: structure, function, and clinical applications. A comprehensive review. Pharmacol Ther 79:129-168.

Dai Z, Peng HB (1998) A role of tyrosine phosphatase in acetylcholine receptor cluster dispersal and formation. J Cell Biol 141:1613-1624.

Dai Z, Luo X, Xie H, Peng HB (2000) The actin-driven movement and formation of acetylcholine receptor clusters. J Cell Biol 150:1321-1334.

DiDomenico BJ, Bugaisky GE, Lindquist S (1982) The heat shock response is self-regulated at both the transcriptional and posttranscriptional levels. Cell 31:593-603.

Dobbins GC, Luo S, Yang Z, Xiong WC, Mei L (2008) alpha-Actinin interacts with rapsyn in agrin-stimulated AChR clustering. Mol Brain 1:18.

Fotedar R, Margolis RL (2015) WISp39 and Hsp90: actin' together in cell migration. Oncotarget 6:17871-17872.

Frasson M, Vitadello M, Brunati AM, La Rocca N, Tibaldi E, Pinna LA, Gorza L, Donella-Deana A (2009) Grp94 is Tyr-phosphorylated by Fyn in the lumen of the endoplasmic reticulum and translocates to Golgi in differentiating myoblasts. Biochim Biophys Acta 1793:239-252.

Geng L, Zhang HL, Peng HB (2009) The formation of acetylcholine receptor clusters visualized with quantum dots. BMC Neurosci 10:80.

Gutierrez T, Simmen T (2014) Endoplasmic reticulum chaperones and oxidoreductases: critical regulators of tumor cell survival and immunorecognition. Front Oncol 4:291.

1102 Haghighi AP, McCabe BD, Fetter RD, Palmer JE, Hom S, Goodman CS (2003) Retrograde control
1103 of synaptic transmission by postsynaptic CaMKII at the Drosophila neuromuscular
1104 junction. Neuron 39:255-267.
1105 Hobson BM (1965) Cold blooded vertebrates, including Xenopus laevis. Food Cosmet Toxicol
1106 3:209-215.
1107 Iwasa K, Nambu Y, Motozaki Y, Furukawa Y, Yoshikawa H, Yamada M (2014) Increased skeletal
1108 muscle expression of the endoplasmic reticulum chaperone GRP78 in patients with
1109 myasthenia gravis. J Neuroimmunol 273:72-76.
1110 Kummer TT, Misgeld T, Lichtman JW, Sanes JR (2004) Nerve-independent formation of a
1111 topologically complex postsynaptic apparatus. J Cell Biol 164:1077-1087.
1112 Lee CW, Zhang H, Geng L, Peng HB (2014) Crosslinking-induced endocytosis of acetylcholine
1113 receptors by quantum dots. PLoS One 9:e90187.
1114 Lee CW, Han J, Bamburg JR, Han L, Lynn R, Zheng JQ (2009) Regulation of acetylcholine receptor
1115 clustering by ADF/cofilin-directed vesicular trafficking. Nat Neurosci 12:848-856.
1116 Li L, Xiong WC, Mei L (2018) Neuromuscular Junction Formation, Aging, and Disorders. Annu
1117 Rev Physiol 80:159-188.
1118 Li L, Cao Y, Wu H, Ye X, Zhu Z, Xing G, Shen C, Barik A, Zhang B, Xie X, Zhi W, Gan L, Su H, Xiong
1119 WC, Mei L (2016) Enzymatic Activity of the Scaffold Protein Rapsyn for Synapse
1120 Formation. Neuron 92:1007-1019.
1121 Li XM, Dong XP, Luo SW, Zhang B, Lee DH, Ting AK, Neiswender H, Kim CH, Carpenter-Hyland E,
1122 Gao TM, Xiong WC, Mei L (2008) Retrograde regulation of motoneuron differentiation
1123 by muscle beta-catenin. Nat Neurosci 11:262-268.
1124 Lin W, Burgess RW, Dominguez B, Pfaff SL, Sanes JR, Lee KF (2001) Distinct roles of nerve and
1125 muscle in postsynaptic differentiation of the neuromuscular synapse. Nature 410:1057-
1126 1064.
1127 Liu B, Staron M, Hong F, Wu BX, Sun S, Morales C, Crosson CE, Tomlinson S, Kim I, Wu D, Li Z
1128 (2013) Essential roles of grp94 in gut homeostasis via chaperoning canonical Wnt
1129 pathway. Proc Natl Acad Sci U S A 110:6877-6882.
1130 Liu J, Xu Y, Stoleru D, Salic A (2012) Imaging protein synthesis in cells and tissues with an alkyne
1131 analog of puromycin. Proceedings of the National Academy of Sciences 109:413.
1132 Luo S, Zhang B, Dong XP, Tao Y, Ting A, Zhou Z, Meixiong J, Luo J, Chiu FC, Xiong WC, Mei L
1133 (2008) HSP90 beta regulates rapsyn turnover and subsequent AChR cluster formation
1134 and maintenance. Neuron 60:97-110.
1135 Marzec M, Eletto D, Argon Y (2012) GRP94: An HSP90-like protein specialized for protein folding
1136 and quality control in the endoplasmic reticulum. Biochim Biophys Acta 1823:774-787.
1137 Murphy N, Bonner HP, Ward MW, Murphy BM, Prehn JH, Henshall DC (2008) Depletion of 14-3-
1138 3 zeta elicits endoplasmic reticulum stress and cell death, and increases vulnerability to
1139 kainate-induced injury in mouse hippocampal cultures. J Neurochem 106:978-988.
1140 Oury J, Liu Y, Töpf A, Todorovic S, Hoedt E, Preethish-Kumar V, Neubert TA, Lin W, Lochmüller H,
1141 Burden SJ (2019) MACF1 links Rapsyn to microtubule- and actin-binding proteins to
1142 maintain neuromuscular synapses. The Journal of cell biology 218:1686-1705.
1143 Peng HB, Baker LP, Chen Q (1991) Tissue culture of Xenopus neurons and muscle cells as a
1144 model for studying synaptic induction. Methods Cell Biol 36:511-526.
1145 Prodromou C (2016) Mechanisms of Hsp90 regulation. Biochem J 473:2439-2452.

1146 Proszynski TJ, Gingras J, Valdez G, Krzewski K, Sanes JR (2009) Podosomes are present in a
1147 postsynaptic apparatus and participate in its maturation. Proc Natl Acad Sci U S A
1148 106:18373-18378.
1149 Richter K, Haslbeck M, Buchner J (2010) The heat shock response: life on the verge of death.
1150 Mol Cell 40:253-266.
1151 Rizzo AM, Adorni L, Montorfano G, Rossi F, Berra B (2007) Antioxidant metabolism of Xenopus
1152 laevis embryos during the first days of development. Comp Biochem Physiol B Biochem
1153 Mol Biol 146:94-100.
1154 Sanes JR, Lichtman JW (2001) Induction, assembly, maturation and maintenance of a
1155 postsynaptic apparatus. Nat Rev Neurosci 2:791-805.
1156 Schopf FH, Biebl MM, Buchner J (2017) The HSP90 chaperone machinery. Nat Rev Mol Cell Biol
1157 18:345-360.
1158 Sharp S, Workman P (2006) Inhibitors of the HSP90 molecular chaperone: current status. Adv
1159 Cancer Res 95:323-348.
1160 Slomnicki LP, Pietrzak M, Vashishta A, Jones J, Lynch N, Elliot S, Poulos E, Malicote D, Morris BE,
1161 Hallgren J, Hetman M (2016) Requirement of Neuronal Ribosome Synthesis for Growth
1162 and Maintenance of the Dendritic Tree. J Biol Chem 291:5721-5739.
1163 Suzuki S, Utsugisawa K, Iwasa K, Satoh T, Nagane Y, Yoshikawa H, Kuwana M, Suzuki N (2011)
1164 Autoimmunity to endoplasmic reticulum chaperone GRP94 in myasthenia gravis. J
1165 Neuroimmunol 237:87-92.
1166 Tsai PI, Wang M, Kao HH, Cheng YJ, Lin YJ, Chen RH, Chien CT (2012) Activity-dependent
1167 retrograde laminin A signaling regulates synapse growth at Drosophila neuromuscular
1168 junctions. Proc Natl Acad Sci U S A 109:17699-17704.
1169 Van PN, Peter F, Soling HD (1989) Four intracisternal calcium-binding glycoproteins from rat
1170 liver microsomes with high affinity for calcium. No indication for calsequestrin-like
1171 proteins in inositol 1,4,5-trisphosphate-sensitive calcium sequestering rat liver vesicles. J
1172 Biol Chem 264:17494-17501.
1173 Vogl AM, Phu L, Becerra R, Giusti SA, Verschueren E, Hinkle TB, Bordenave MD, Adrian M,
1174 Heidersbach A, Yankilevich P, Stefani FD, Wurst W, Hoogenraad CC, Kirkpatrick DS,
1175 Refojo D, Sheng M (2020) Global site-specific neddylation profiling reveals that
1176 NEDDylated cofilin regulates actin dynamics. Nat Struct Mol Biol 27:210-220.
1177 Wang ZZ, Mathias A, Gautam M, Hall ZW (1999) Metabolic stabilization of muscle nicotinic
1178 acetylcholine receptor by rapsyn. J Neurosci 19:1998-2007.
1179 Xing G, Xiong WC, Mei L (2020) Rapsyn as a signaling and scaffolding molecule in neuromuscular
1180 junction formation and maintenance. Neurosci Lett 731:135013.
1181 Yang X, Li W, Prescott ED, Burden SJ, Wang JC (2000) DNA topoisomerase IIbeta and neural
1182 development. Science 287:131-134.
1183 Yang X, Arber S, William C, Li L, Tanabe Y, Jessell TM, Birchmeier C, Burden SJ (2001) Patterning
1184 of muscle acetylcholine receptor gene expression in the absence of motor innervation.
1185 Neuron 30:399-410.
1186 Yeates CJ, Zwiefelhofer DJ, Frank CA (2017) The Maintenance of Synaptic Homeostasis at the
1187 Drosophila Neuromuscular Junction Is Reversible and Sensitive to High Temperature.
1188 eNeuro 4.

1189 Yeo HL, Lim JY, Fukami Y, Yuki N, Lee CW (2015) Using Xenopus tissue cultures for the study of
1190 myasthenia gravis pathogenesis. Dev Biol 408:244-251.
1191 Zhu Y, de Castro L, Cooper RL (2018) Effect of temperature change on synaptic transmission at
1192 crayfish neuromuscular junctions. Biol Open 7.
1193

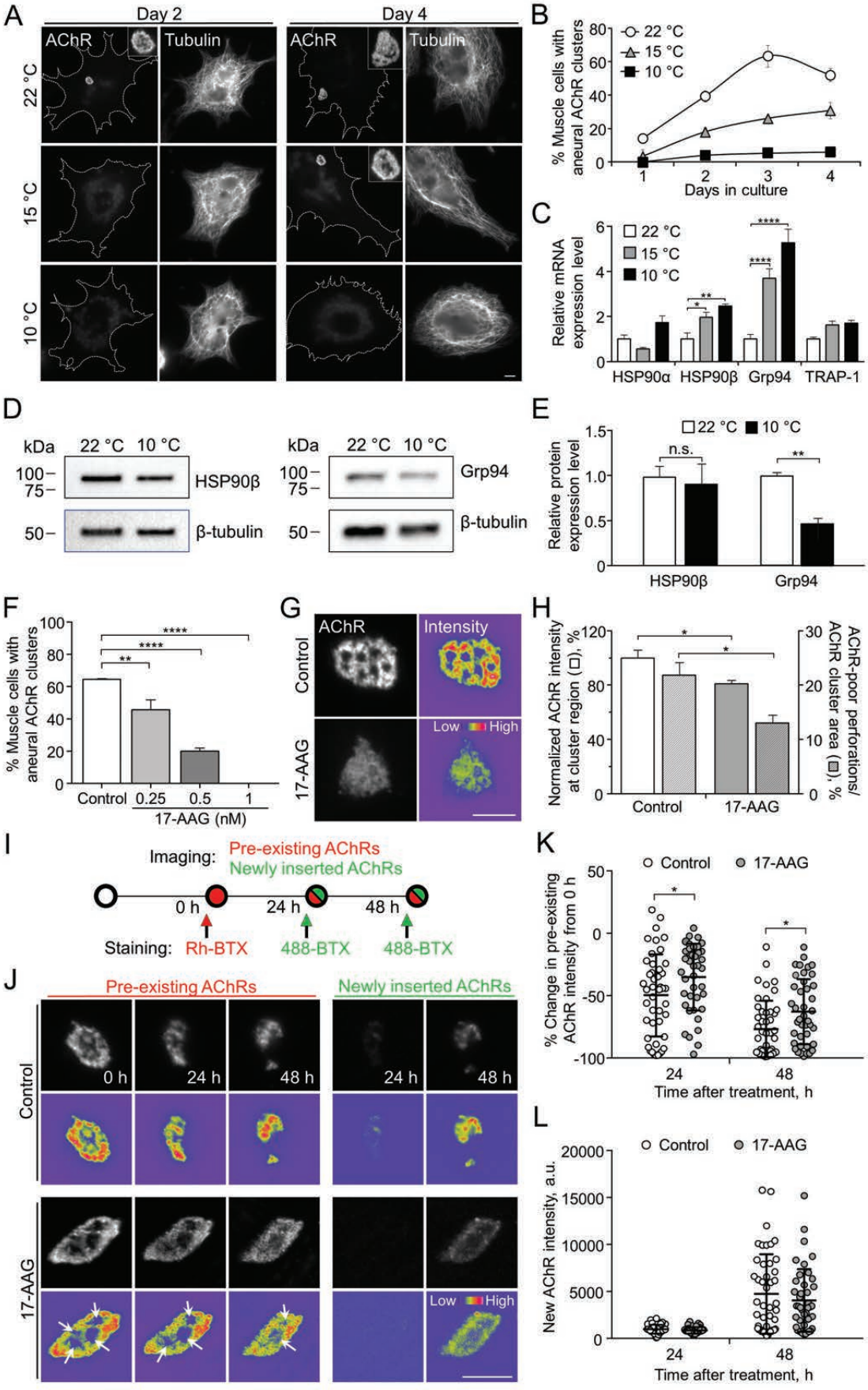

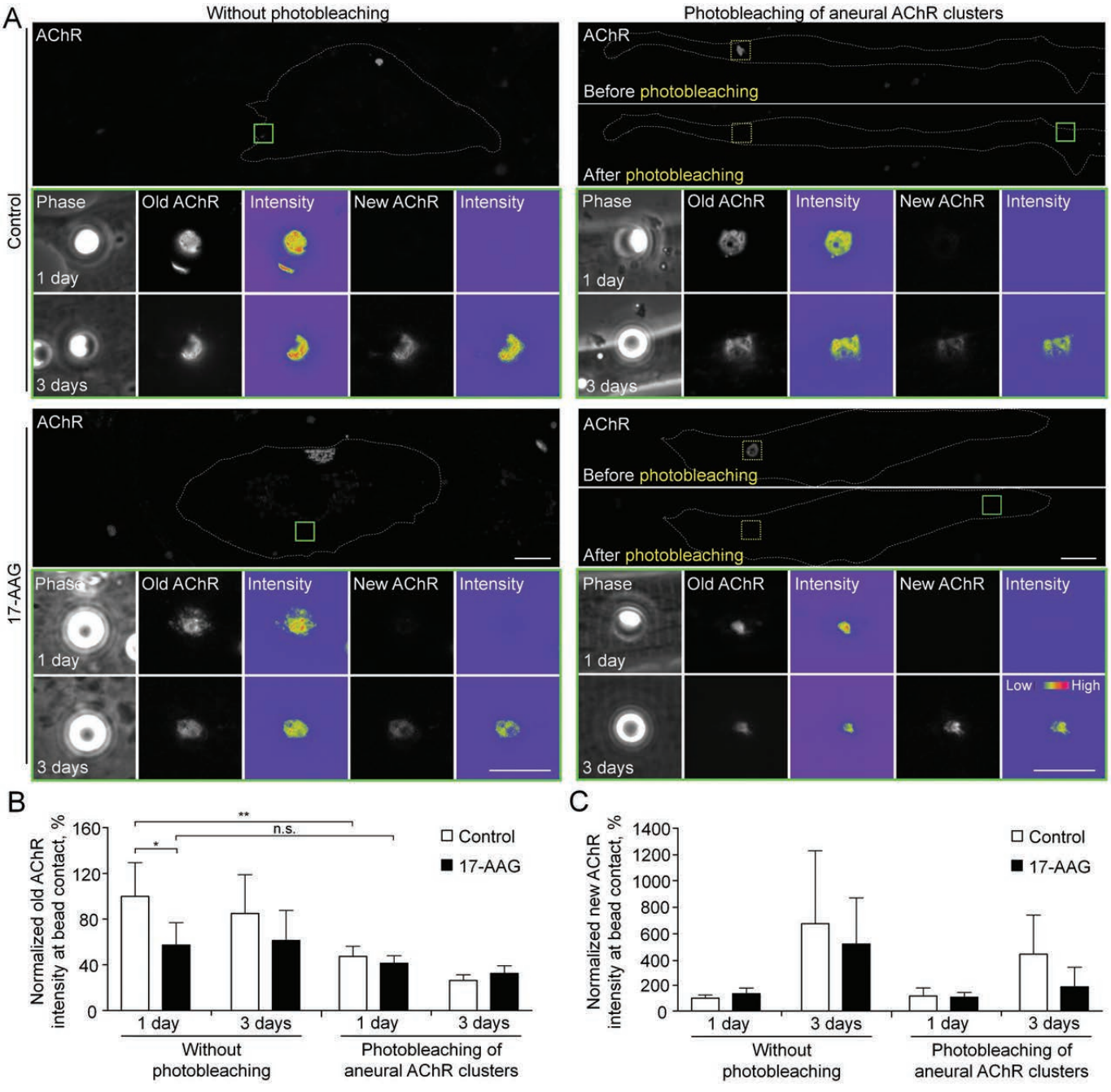

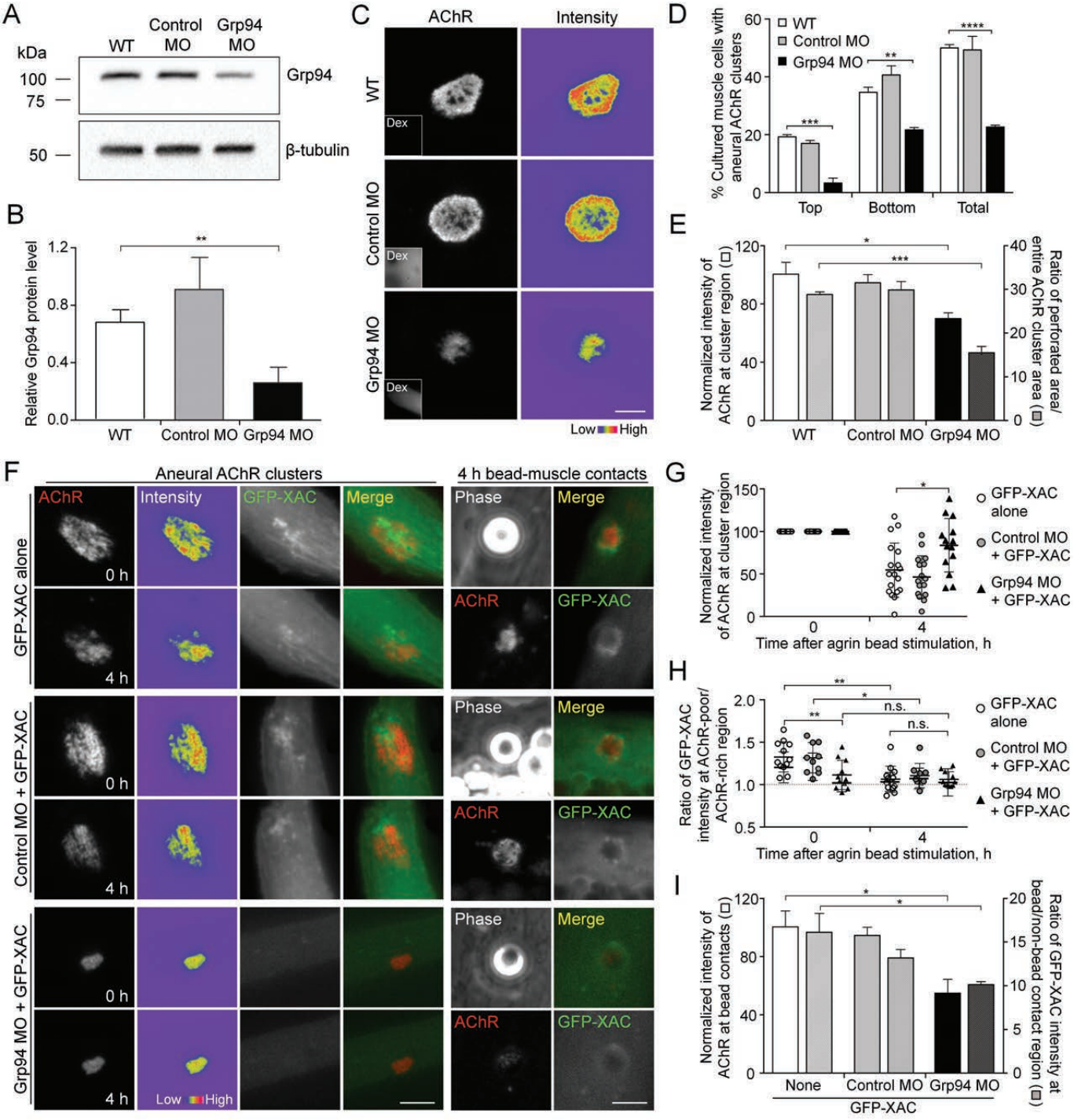

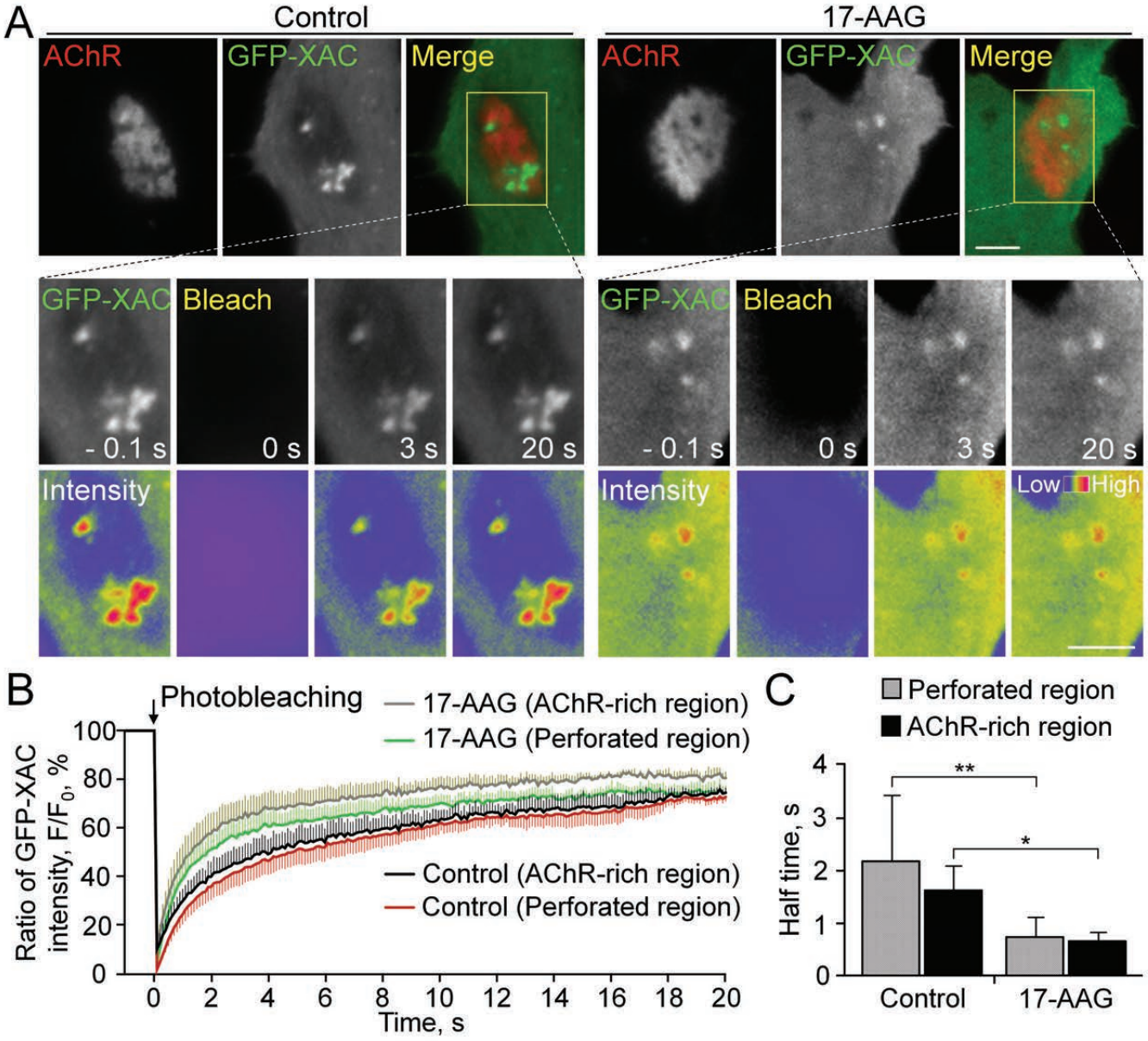

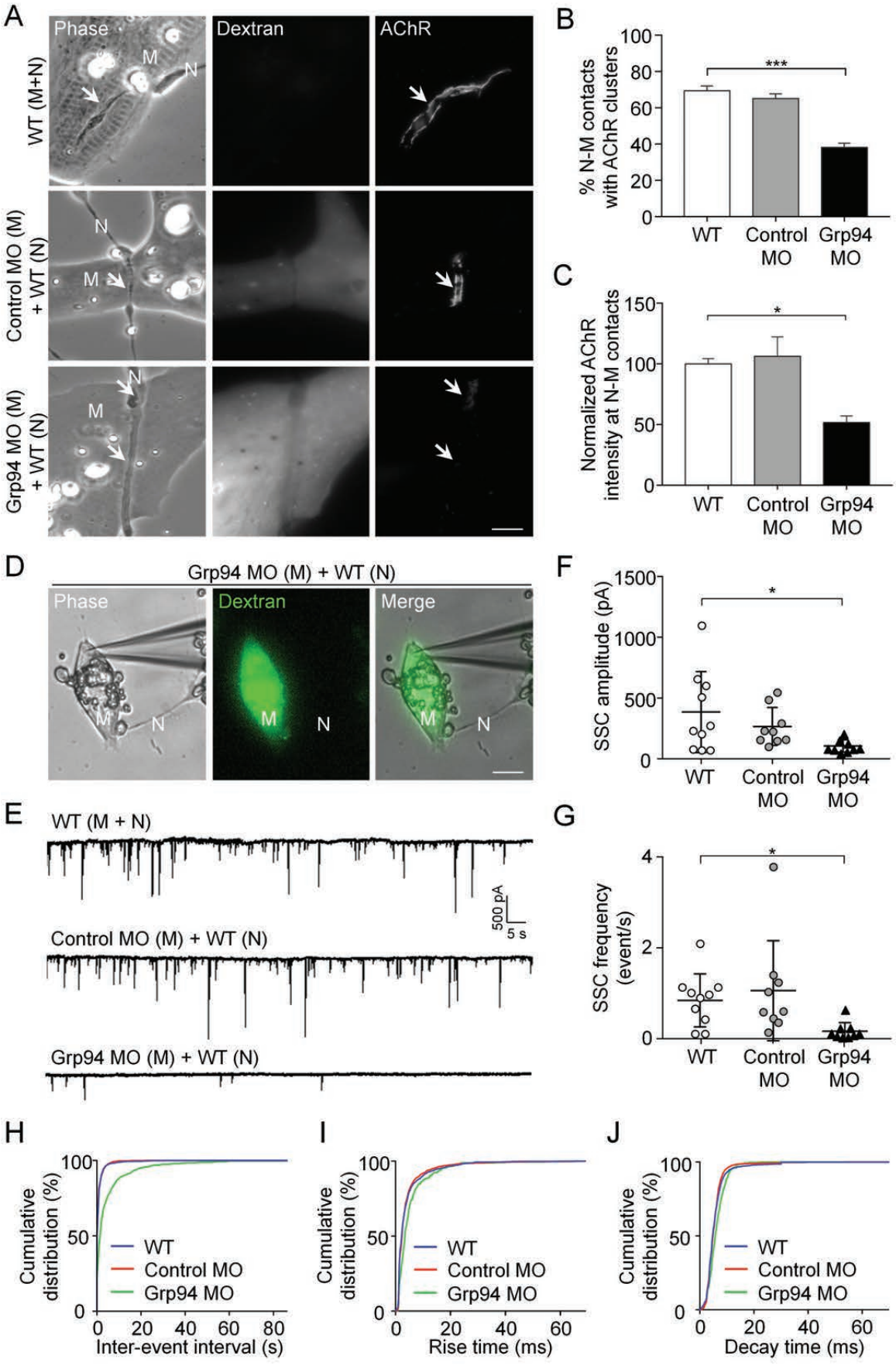

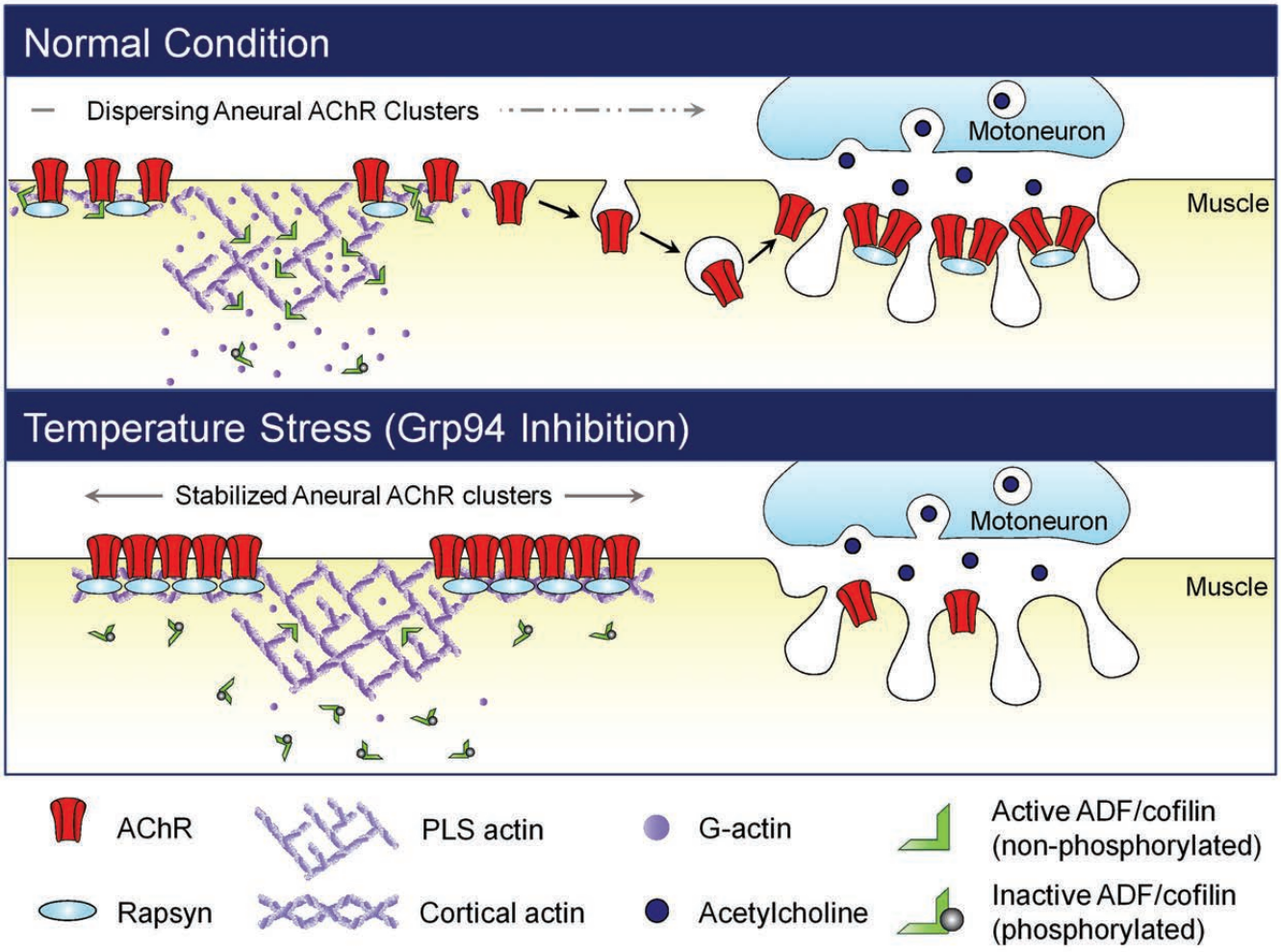

Figures	Comparison		Statistical test	p-value	F, Dfn, Dfd
1B	1 Day	22 °C vs. 15 °C	Two-way ANOVA, Turkey's multiple comparison test	0.0163	Interaction: 15.96, 6, 18; Time point: 71.17, 3, 18; Temperature: 142.8, 2, 6
		22 °C vs. 10 °C		0.0019	
	2 Day	22 °C vs. 15 °C		0.0001	
		22 °C vs. 10 °C		0.0001	
	3 Day	22 °C vs. 15 °C		0.0001	
		22 °C vs. 10 °C		0.0001	
	4 Day	22 °C vs. 15 °C		0.0001	
		22 °C vs. 10 °C		0.0001	
1C	HSP90α	22 °C vs. 15 °C	Two-way ANOVA, Turkey's multiple comparison test	0.5097	Interaction: 11.22, 6, 24; Gene: 38.81, 3, 24; Temperature: 43.31, 2, 24
		22 °C vs. 10 °C		0.159	
		15 °C vs. 10 °C		0.0155	
	HSP90β	22 °C vs. 15 °C		0.0489	
		22 °C vs. 10 °C		0.0024	
		15 °C vs. 10 °C		0.4152	
	Grp94	22 °C vs. 15 °C		<0.0001	
		22 °C vs. 10 °C		<0.0001	
		15 °C vs. 10 °C		0.0012	
	TRAP-1	22 °C vs. 15 °C		0.2602	
		22 °C vs. 10 °C		0.1889	
		15 °C vs. 10 °C		0.9793	
1E	HSP90β	22 °C vs. 10 °C	Unpaired t test with Welch's correction	0.7421	4.39, 2, 2
	Grp94	22 °C vs. 10 °C		0.0035	3.03, 2, 2
1F		Control vs. 0.25nM	One-way ANOVA, Turkey's multiple comparison test	0.0067	75.47, 3, 12
		Control vs. 0.5nM		<0.0001	
		Control vs. 1nM		<0.0001	
1H	Normalized AChR intensity cluster region	Control vs. 17-AAG	Unpaired t test	0.0403	4.762, 2, 2

	AChR-poor perforations/AChR cluster area		Unpaired t test	0.02	2.462, 3, 3
1K	24 h	Control vs. 17-AAG	Two-way ANOVA, Sidak's multiple comparison test	0.0274	Interaction: 0.02911, 1, 85; Treatment: 151.1, 1, 85; Time point: 6.856, 1, 85
	48 h			0.0385	
1L	24 h	Control vs. 17-AAG	Two-way ANOVA, Sidak's multiple comparison test	0.9726	Interaction: 0.5439, 1, 86; Treatment: 80.21, 1, 86; Time point: 6.856, 1, 85
	48 h			0.4136	
1-1B	Polar metabolites	Control vs. 17-AAG	Unpaired t test	Listed in Table 1-1	N/A
1-1D	Fatty acids		Unpaired t test	Listed in Table 1-2	N/A
1-1F		Control vs. CHX	One-way ANOVA, Dunnett's multiple comparison test	0.0142	9.046, 2, 6
		Control vs. 17-AAG		0.8498	
1-1H		Control vs. 17-AAG	Unpaired t test with Welch's correction	0.3747	1.388, 32, 41
2B	1 day - Without :Control vs. 1 day - Without :17-AAG		Two-way ANOVA, Turkey's multiple comparison test	0.0198	Interaction: 6.99, 3, 6; Treatment: 6.916, 1, 2; Time point: 10.88, 3, 6
	1 day - Without :Control vs. 3 days - Without :Control			0.6093	
	1 day - Without :Control vs. 3 days - Without :17-AAG			0.0318	
	1 day - Without :Control vs. 1 day - Photobleaching of aneural AChR cluster:Control			0.0069	
	1 day - Without :Control vs. 1 day - Photobleaching of aneural AChR cluster:17-AAG			0.004	
	1 day - Without :Control vs. 3 days - Photobleaching of aneural AChR cluster:Control			0.0011	
	1 day - Without :Control vs. 3 days - Photobleaching of aneural AChR cluster:17-AAG			0.0018	

	1 day - Without :17-AAG vs. 3 days - Without :Control		0.126	
	1 day - Without :17-AAG vs. 3 days - Without :17-AAG		0.9991	
	1 day - Without :17-AAG vs. 1 day - Photobleaching of aneural AChR cluster:Control		0.8927	
	1 day - Without :17-AAG vs. 1 day - Photobleaching of aneural AChR cluster:17-AAG		0.5569	
	1 day - Without :17-AAG vs. 3 days - Photobleaching of aneural AChR cluster:Control		0.0818	
	1 day - Without :17-AAG vs. 3 days - Photobleaching of aneural AChR cluster:17-AAG		0.1828	
	3 days - Without :Control vs. 3 days - Without :17-AAG		0.2166	
	3 days - Without :Control vs. 1 day - Photobleaching of aneural AChR cluster:Control		0.0356	
	3 days - Without :Control vs. 1 day - Photobleaching of aneural AChR cluster:17-AAG		0.018	
	3 days - Without :Control vs. 3 days - Photobleaching of aneural AChR cluster:Control		0.004	
	3 days - Without :Control vs. 3 days - Photobleaching of aneural AChR cluster:17-AAG		0.007	
	3 days - Without :17-AAG vs. 1 day - Photobleaching of aneural AChR cluster:Control		0.6672	
	3 days - Without :17-AAG vs. 1 day - Photobleaching of aneural AChR cluster:17-AAG		0.3446	
	3 days - Without :17-AAG vs. 3 days - Photobleaching of aneural AChR cluster:Control		0.0487	
	3 days - Without :17-AAG vs. 3 days - Photobleaching of aneural AChR cluster:17-AAG		0.1064	
	1 day - Photobleaching of aneural AChR cluster:Control vs. 1 day - Photobleaching of aneural AChR cluster:17-AAG		0.9916	
	1 day - Photobleaching of aneural AChR cluster:Control vs. 3 days - Photobleaching of aneural AChR cluster:Control		0.3032	
	1 day - Photobleaching of aneural AChR cluster:Control vs. 3 days - Photobleaching of aneural AChR cluster:17-AAG		0.6183	
	1 day - Photobleaching of aneural AChR cluster:17-AAG vs. 3 days - Photobleaching of aneural AChR cluster:Control		0.6054	

	1 day - Photobleaching of aneural AChR cluster:17-AAG vs. 3 days - Photobleaching of aneural AChR cluster:17-AAG		0.9315	
	3 days - Photobleaching of aneural AChR cluster:Control vs. 3 days - Photobleaching of aneural AChR cluster:17-AAG		0.9898	
2C	1 day - Without :Control vs. 1 day - Without :17-AAG	Two-way ANOVA, Turkey's multiple comparison test	>0.9999	Interaction: 0.293, 3, 6; Treatment: 0.2994, 1, 2; Time point: 11.74, 3, 6
	1 day - Without :Control vs. 3 days - Without :Control		0.406	
	1 day - Without :Control vs. 3 days - Without :17-AAG		0.6936	
	1 day - Without :Control vs. 1 day - Photobleaching of aneural AChR cluster:Control		>0.9999	
	1 day - Without :Control vs. 1 day - Photobleaching of aneural AChR cluster:17-AAG		>0.9999	
	1 day - Without :Control vs. 3 days - Photobleaching of aneural AChR cluster:Control		0.832	
	1 day - Without :Control vs. 3 days - Photobleaching of aneural AChR cluster:17-AAG		0.9999	
	1 day - Without :17-AAG vs. 3 days - Without :Control		0.4594	
	1 day - Without :17-AAG vs. 3 days - Without :17-AAG		0.7563	
	1 day - Without :17-AAG vs. 1 day - Photobleaching of aneural AChR cluster:Control		>0.9999	
	1 day - Without :17-AAG vs. 1 day - Photobleaching of aneural AChR cluster:17-AAG		>0.9999	
	1 day - Without :17-AAG vs. 3 days - Photobleaching of aneural AChR cluster:Control		0.8826	
	1 day - Without :17-AAG vs. 3 days - Photobleaching of aneural AChR cluster:17-AAG		>0.9999	
	3 days - Without :Control vs. 3 days - Without :17-AAG		0.9968	
	3 days - Without :Control vs. 1 day - Photobleaching of aneural AChR cluster:Control		0.4322	
	3 days - Without :Control vs. 1 day - Photobleaching of aneural AChR cluster:17-AAG		0.4267	
	3 days - Without :Control vs. 3 days - Photobleaching of aneural AChR cluster:Control		0.9722	
	3 days - Without :Control vs. 3 days - Photobleaching of aneural AChR cluster:17-AAG		0.5671	
	3 days - Without :17-AAG vs. 1 day - Photobleaching of aneural AChR cluster:Control		0.7253	
	3 days - Without :17-AAG vs. 1 day - Photobleaching of aneural AChR cluster:17-AAG		0.7188	

	3 days - Without :17-AAG vs. 3 days - Photobleaching of aneural AChR cluster:Control			>0.9999	
	3 days - Without :17-AAG vs. 3 days - Photobleaching of aneural AChR cluster:17-AAG			0.8595	
	1 day - Photobleaching of aneural AChR cluster:Control vs. 1 day - Photobleaching of aneural AChR cluster:17-AAG			>0.9999	
	1 day - Photobleaching of aneural AChR cluster:Control vs. 3 days - Photobleaching of aneural AChR cluster:Control			0.8583	
	1 day - Photobleaching of aneural AChR cluster:Control vs. 3 days - Photobleaching of aneural AChR cluster:17-AAG			>0.9999	
	1 day - Photobleaching of aneural AChR cluster:17-AAG vs. 3 days - Photobleaching of aneural AChR cluster:Control			0.853	
	1 day - Photobleaching of aneural AChR cluster:17-AAG vs. 3 days - Photobleaching of aneural AChR cluster:17-AAG			>0.9999	
	3 days - Photobleaching of aneural AChR cluster:Control vs. 3 days - Photobleaching of aneural AChR cluster:17-AAG			0.9511	
3B		WT vs. Control MO	One-way ANOVA, Dunnett's multiple comparison test	0.1383	21.35, 2,
		WT vs. Grp94 MO		0.0089	
3D	Top	WT vs. Control MO	Two-way ANOVA, Turkey's multiple comparison test	0.7282	Interaction: 4.283, 4, 18; Treatment: 127.9, 2, 18; Cluster type: 80.22, 2, 18
		WT vs. Grp94 MO		0.0002	
		Control MO vs. Grp94 MO		0.0008	
	Bottom	WT vs. Control MO		0.1487	
		WT vs. Grp94 MO		0.0013	
		Control MO vs. Grp94 MO		<0.0001	
	Total	WT vs. Control MO		0.974	
		WT vs. Grp94 MO		<0.0001	
		Control MO vs. Grp94 MO		<0.0001	
3E	Normalized intensity of AChR at cluster region	WT vs. Control MO	One-way ANOVA, Dunnett's multiple	0.7416	6.557, 2, 9
		WT vs. Grp94 MO		0.0141	
	Ratio of perforated area/	WT vs. Control MO		0.8166	31.46, 2, 9

	entire AChR cluster area	WT vs. Grp94 MO	comparison test	0.0002	
3G		XAC-GFP vs. XAC-GFP + Control MO	Two-way ANOVA, Sidak's multiple comparison test	0.6801	Interaction: 6.469, 2, 45; Treatment: 80.39, 1, 45; Time point: 6.469, 2, 45
		XAC-GFP vs. XAC-GFP + Grp94 MO		0.0162	
3I	Normalized intensity of AChR at bead contacts	XAC-GFP alone vs. XAC-GFP + Control MO	One-way ANOVA, Turkey's multiple comparison test	0.8926	6.716, 2, 9
		XAC-GFP alone vs. XAC-GFP + Grp94 MO		0.0201	
		XAC-GFP + Control MO vs. XAC-GFP + Grp94 MO		0.0409	
	Ratio of GFP-XAC intensity at bead/non-bead contact region	XAC-GFP alone vs. XAC-GFP + Control MO		0.3488	4.59, 2, 9
		XAC-GFP alone vs. XAC-GFP + Grp94 MO		0.0345	
		XAC-GFP + Control MO vs. XAC-GFP + Grp94 MO		0.3109	
3H	0 h	GFP-XAC alone vs. Control MO + GFP-XAC	Two-way ANOVA, Sidak's multiple comparison test	0.9862	Interaction: 2.583, 2, 29; Treatment: 18.65, 1, 29; Time point: 4.2, 2, 29
		GFP-XAC alone vs. Grp94 MO + GFP-XAC		0.0038	
	4 h	GFP-XAC alone vs. Control MO + GFP-XAC		0.7729	
		GFP-XAC alone vs. Grp94 MO + GFP-XAC		0.9996	
	GFP-XAC alone	0 h vs. 4 h		0.0012	
	Control MO + GFP-XAC			0.0299	
	Grp94 MO + GFP-XAC			0.8305	
3-1B	XAC	WT vs. Control Mo	One-way	0.1955	12.16, 2, 9

		WT vs. Grp94 Mo	ANOVA, Dunnett's multiple comparison test	0.0016	
3-1C	p34-Arc	WT vs. Control Mo		0.9667	7.445, 2, 6
		WT vs. Grp94 Mo		0.0242	
3-1D	Vinculin	WT vs. Control Mo		0.8551	5.924, 2, 6
		WT vs. Grp94 Mo		0.0331	
4C	Perforated region	Control vs. 17-AAG	Unpaired t test with Welch's correction	0.0025	11.1, 11, 5
	AChR-rich region	Control vs. 17-AAG		0.049	11.64, 10, 5
4-1C	Perforated region	GFP-XAC vs. GFP-XAC (S3A)	One-way ANOVA, Turkey's multiple comparison test	0.1195	16.04, 2, 27
		GFP-XAC vs. GFP-XAC (S3E)		0.0015	
		GFP-XAC (S3A) vs. GFP-XAC (S3E)		<0.0001	
	AChR-rich region	GFP-XAC vs. GFP-XAC (S3A)		0.0025	16.9, 2, 27
		GFP-XAC vs. GFP-XAC (S3E)		0.0497	
		GFP-XAC (S3A) vs. GFP-XAC (S3E)		<0.0001	
5B		WT vs. Control MO	One-way ANOVA, Turkey's multiple comparison test	0.511	44.59, 2, 6
		WT vs. Grp94 MO		0.0003	
		Control MO vs. Grp94 MO		0.0007	
5C		WT vs. Control MO	One-way ANOVA, Turkey's multiple comparison test	0.9022	8.63, 2, 6
		WT vs. Grp94 MO		0.0351	
		Control MO vs. Grp94 MO		0.0211	
5F		WT vs. Control MO	Kruskal–Wallis ANOVA test with Dunn's multiple comparison test	N/A	N/A
		WT vs. Grp94 MO			
		Control MO vs. Grp94 MO			
5G		WT vs. Control MO	Kruskal–Wallis ANOVA test with Dunn's multiple comparison test		
		WT vs. Grp94 MO			
		Control MO vs. Grp94 MO			
5-1B		Control vs. 17-AAG	One-way ANOVA,	0.0009	13.85, 4, 11
		Control vs. PU-WS13		0.0074	

		Control vs. Control MO	Dunnett's multiple comparison test	0.8996	
		Control vs. Grp94 MO		0.0004	
5-1C		Control vs. 17-AAG		0.0195	5.745, 4, 11
		Control vs. PU-WS13		0.0233	
		Control vs. Control MO		0.9971	
		Control vs. Grp94 MO		0.0329	
5-2B	0.5 h	Control vs. 17-AAG	One-way ANOVA, Dunnett's multiple comparison test	0.0001	9.548, 2, 74
		Control vs. PU-WS13		0.0154	
	4 h	Control vs. 17-AAG		0.0001	20.28, 2, 73
		Control vs. PU-WS13		0.0001	